THE JOURNAL OF PHYSICAL CHEMISTRY C

Article

Cite This: J. Phys. Chem. C 2018, 122, 10006−10016

pubs.acs.org/JPCC

Au Dendrite Electrocatalysts for CO_2 Electrolysis

Nathan T. Nesbitt,*[,†] Ming Ma,[‡] Bartek J. Trześniewski,[‡] Samantha Jaszewski,[†] Fazel Tafti,[†] Michael J. Burns,[†] Wilson A. Smith,*[,‡] and Michael J. Naughton*[,†]

[†]Department of Physics, Boston College, Chestnut Hill, Massachusetts 02467, United States

[‡]Materials for Energy Conversion and Storage (MECS), Department of Chemical Engineering, Faculty of Applied Sciences, Delft University of Technology, 2629 HZ Delft, The Netherlands

Supporting Information

ABSTRACT: Electrochemical CO_2 reduction can convert CO_2 into fuels and valuable chemicals using renewable electricity, which provides a prospective path toward large-scale energy storage. Au nanostructured electrodes have demonstrated the best catalytic performance for CO_2 conversion: high catalytic selectivity for CO formation at low overpotentials, high current density, and long-term durability. Here, we report selective electrocatalytic CO_2 reduction to CO on nanostructured Au with various morphologies, prepared via electrocrystallization with a megahertz potential oscillation. X-ray diffraction showed that the proportion of {100} and {110} to {111} surfaces increased at more negative deposition potentials. Cyclic voltammetry showed the potential of zero charge on an Au film was approximately 0.35 V vs standard hydrogen electrode (SHE) and that the surface energy decreased by ∼1 eV/nm^2 at −0.5 V vs SHE, tending to 0 within several volts in either direction. Scanning electron micrograms showed that the Au crystals grow primarily in the ⟨110⟩ directions. From these data, a model for crystallization from melts was adapted to calculate the roughening temperature of the {111}, {100}, and {110} Miller indices as 7000, 4000, and 1000 K, decreasing for more negative deposition potentials. This offers a framework for exposed facet control in electrocrystallization. In CO_2 electrocatalysis, −0.35 V vs reversible hydrogen electrode was observed to be a turn-on potential for improved CO_2 reduction activity; dendrites showed 50% Faradaic efficiency for CO production at more cathodic potentials. The Tafel slope was measured to be 40 mV/decade for {100} and {110}-rich Au dendrites and 110 mV/decade for {111}-dominated Au plates, suggesting the higher surface energy crystal facets may stabilize all of the CO_2 reduction reaction intermediates.

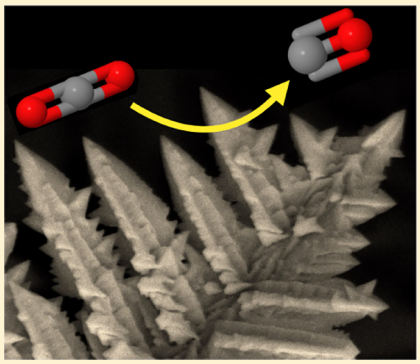

INTRODUCTION

Rapidly falling electricity prices from renewable sources, such as wind and solar, show promise to provide society with cheap domestic energy, while also mitigating the adverse human health impacts of anthropogenic climate change and pollution from fossil fuel extraction and utilization. These energy sources are generally intermittent and thus require energy storage technology for full deployment. Electrochemical CO_2 reduction may provide a means for large-scale storage of renewable electrical energy in hydrocarbon fuels, which are relatively inexpensive to store and are compatible with much of the world's existing infrastructure.

In this study, the CO_2 reduction reaction (CO_2RR) takes place at a metal catalyst immersed in an aqueous electrolyte: 0.5 M $NaHCO_3$ saturated with CO_2. The desired product is CO, produced in the reaction

$$CO_2 + 2H^+ + 2e^- \rightarrow CO + H_2O\ (-0.11\text{V vs. RHE}) \quad (1)$$

Thorough studies have been reported on the electrocatalytic performance of flat films of various metals that are selective for the formation of CO.[1,2] These results showed Au to have the best catalytic performance, as it demonstrated the highest values for three important parameters of electrocatalysts: activity (reaction rate per given overpotential (η)), selectivity (percent of the total products generated that were the desired chemical), and stability (constant performance over time). The potential (φ) of −0.35 V vs reversible hydrogen electrode (V_{RHE}) is convenient for comparing the performance of Au catalysts; it is slightly more cathodic than the onset of cathodic current on Au films, and it has a reasonable energy efficiency of 85% for the partial current directed to CO production (energy efficiency = $E^0/(E^0 + \eta)$ = (1.34 V)/(1.34 V + 0.24 V) = 0.85). This only considers energy losses at the cathode, ignoring losses present at the anode, which can be separately mitigated via reactor engineering and using specialty membranes.[3] At this low overpotential of 0.24 V, polycrystalline Au films have been shown to produce only ∼10 μA/cm^2 total current density (j_{total}) at nearly 0% Faradaic efficiency for CO (H_2 was the primary product).[4] However, recent studies have found nanostructuring Au significantly improves its performance. Specifically, in 2012, an Au nanoparticle film was produced by

Received: February 22, 2018
Revised: April 13, 2018
Published: April 19, 2018

DOI: 10.1021/acs.jpcc.8b01831
J. Phys. Chem. C 2018, 122, 10006−10016

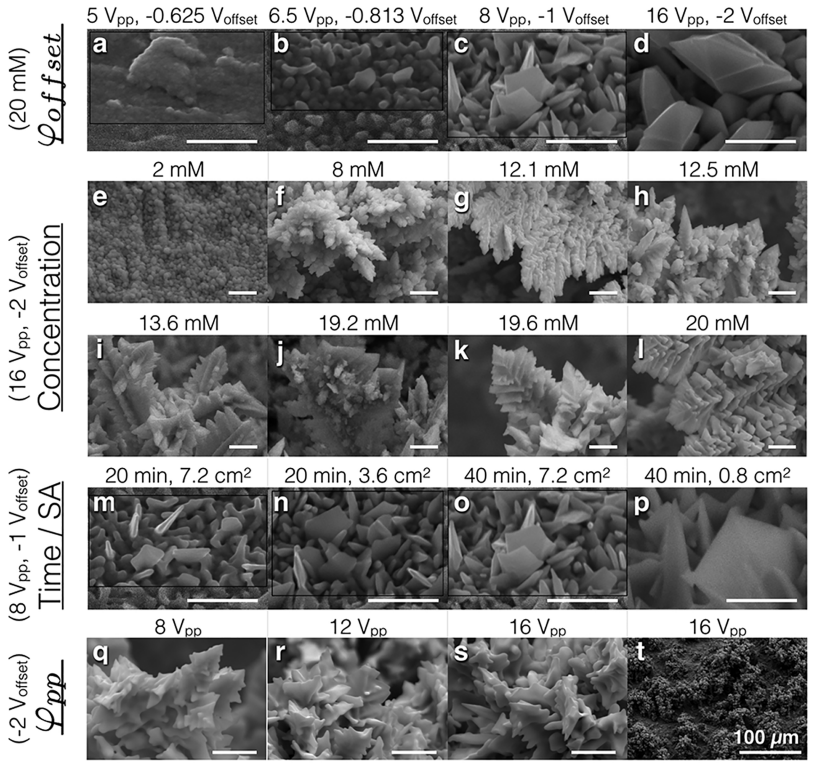

Figure 1. Representative SEMs of Au crystals grown in various conditions. In all cases, a 20 MHz square wave was applied between the sample and a Pt wire spiral CE, separated by approximately 20 mm and immersed in 20 mL of solution. For (a–p), $\varphi_{pp} = 8\ \varphi_{offset}$. (a–d) For the electric potential study, there were 40 min of deposition to a geometric surface area of 3.6 cm^2 from approximately 20 mM $HAuCl_4$; φ_{offset} was varied from −0.625 to −2 V. (e–l) For the concentration study, $\varphi_{offset} = -2$ V was applied for 40 min to a geometric surface area of 0.8 cm^2, and the molarity of $HAuCl_4$ was varied from 2 to 20 mM. (m–p) For the time and surface area study, $\varphi_{offset} = -1$ V was applied with approximately 20 mM $HAuCl_4$, while the time was varied from 20 to 40 min and the geometric surface area from 7.2 to 0.8 cm^2. (q–t) For the φ_{pp} study, $\varphi_{offset} = -2$ V was applied for 40 min to a geometric surface area of 0.8 cm^2 with approximately 20 mM $HAuCl_4$, and φ_{pp} was varied between 8, 12, and 16 V. Scale bars are 1 μm unless otherwise indicated.

repeated electrochemical oxidation and reduction of a polycrystalline Au film.[4] The nanoparticle film showed improved performance over both a planar film and a film of commercially available nanoparticles. It produced about $j_{total} = 2$ mA/cm^2 at over 96% Faradaic efficiency for CO.[4] This suggested there was a special quality of the electrochemically reduced surface that improved catalytic performance. In 2016, direct current (DC) electrodeposition of Au nanoneedles was shown to produce about $j_{total} = 15$ mA/cm^2 at over 95% Faradaic efficiency for CO at the same applied potential.[5,6] It was suggested that the high performance was a result of enhanced electric fields at the needles' sharp tips. This was the first and only report to date of a 40 mV/dec Tafel slope for the CO_2RR on Au, which corresponds to stabilizing all the reaction intermediates in several proposed reaction schemes.[2]

In light of the positive results of electrochemically produced nanostructures of Au, here we tested a technique for the growth of nanoscale Au dendrites and Au plates from an aqueous $HAuCl_4$ solution with a megahertz (MHz) square-wave potential oscillation and a DC offset potential.[7−11] Different electrodeposition conditions were found to produce different proportions of exposed facets on Au dendrites and plates. Scanning electron microscopy (SEM), transmission electron microscopy (TEM), and X-ray diffraction spectroscopy (XRD) were used to determine the crystallographic orientation of the Au surfaces. X-ray photoelectron spectroscopy (XPS) was used to determine the composition. Electrochemical impedance spectroscopy (EIS) was used to measure the change in surface energy (γ) vs φ in various aqueous solutions. An electrochemical cell, potentiostat, and gas chromatograph (GC) were used to measure the performance of the nanostructures as electrocatalysts for CO_2 reduction. The purpose of this study was to understand the nanostructure growth mechanism and thereby provide a platform for rational design of future nanostructures. Our results were compared to existing models for crystallization from aqueous solutions and metal melts to identify common trends. Correlations between nanostructure morphology and catalytic performance offer a pathway for improved structure functionality relationships for nanostructured electrocatalysts used in CO_2 reduction.

EXPERIMENTAL METHODS

Au Crystal Synthesis. To grow the Au dendrites and plates, a two-electrode setup was used. The counter electrode was a Pt wire spiral. The working electrode was a 2 × 2 × 0.1 cm Ti foil chip, sputter coated on the front with 100 nm of Au. The back of the Ti foil was covered by scotch tape, and for samples tested for CO_2RR, the front was covered by Teflon tape with a 1 cm diameter hole for the electrodeposition. Scotch tape was used on the back for easy removal for subsequent experiments. The electrodes were immersed into a small beaker with 20 mL of 2 to 20 mM $HAuCl_4$ in deionized water. A function generator was used to apply a 20 MHz square-wave electric potential between the electrodes, with $\varphi_{offset} = -0.625$ to −2 V and $\varphi_{pp} = 8\varphi_{offset}$. An oscilloscope was attached in parallel to the electrodes to measure the waveform

DOI: 10.1021/acs.jpcc.8b01831
J. Phys. Chem. C 2018, 122, 10006−10016

of the applied potential. Measurements of the current passing through the circuit were not made to avoid modifying the waveform of the high frequency applied potential.

XRD. XRD was performed using a Bruker D8 ECO in the Bragg−Brentano geometry with a copper X-ray source (Cu Kα), a nickel filter to absorb the Kβ radiation, a 2.5° Soller slit after the source, and a 2.5° Soller slit before the LYNXEYE XE 1-D energy dispersive detector. Intensity data were collected in the 2θ range between 5 and 70° with sample rotation.

TEM. Samples were prepared for TEM by scratching the sample surface with a knife, sonicating the sample in isopropanol to suspend small pieces of dendrites or plates, and drop-casting the suspension onto a Ted Pella 01890-F grid (Lacey Carbon Type-A, 300 mesh, copper with an approximate grid hole size of 63 μm). Images were taken with a JEOL 2010F TEM.

EIS. A typical three electrode setup was used with a Gamry Interface 1000 potentiostat. The working electrode was the Au sample, the reference electrode was Ag/AgCl in saturated KCl solution, and the counter electrode was an Au wire spiral. All three electrodes were immersed into a 25 mL beaker containing the electrolyte under study. All electrolytes were prepared with deionized water.

Cyclic Voltammetry Surface Area Measurement. A typical three electrode setup was used with a Gamry Interface 1000 potentiostat. The working electrode was the Au sample, the reference electrode was Ag/AgCl in saturated KCl solution, and the counter electrode was a Pt or Au wire spiral. All three electrodes were immersed into a 80 mL crystallization dish containing either 500 or 375 mM H_2SO_4. Electrolytes were prepared from pure sulfuric acid and deionized water.

XPS. XPS was performed using the Thermo Scientific K-alpha apparatus equipped with an Al Kα X-ray source and a flood gun. Parameters used for the measurements were a spot size of 400 μm, pass energy of 50 eV, energy step size of 0.1 eV, dwell time of 50 ms, and 20 scans in the vicinity of Au 4f and O 1s orbitals' binding energies.

CO_2 Reduction. A typical three electrode setup was used with a Princeton Applied Research VersaSTAT 3. The metal catalyst was the working electrode, the reference electrode was Ag/AgCl in saturated KCl solution, and the counter electrode was a platinum mesh. A Nafion membrane separated the counter electrode from the working and reference electrodes. The electrolyte was deionized water with 0.25 M Na_2CO_3, which after CO_2 was bubbled through it for 30 min was considered 0.5 M $NaHCO_3$. CO_2 was continuously bubbled through the catholyte at 6 sccm and the anolyte at 20 sccm. The gas stream from the catholyte was passed through the gas chromatograph (Thermo Scientific TRACE 1310) to measure the product gas concentration. Both electrolytes were stirred by magnetic stir bars.

RESULTS

Crystal Growth and Morphology. To survey the crystal morphologies produced by this deposition process, the following parameters were varied across a number of samples: offset potential (φ_{offset}), peak-to-peak amplitude (φ_{pp}), $HAuCl_4$ concentration, and Coulombs of deposition per unit area. Figure 1a−d shows the effect of a different φ_{offset}, with the ratio of $\varphi_{pp} = 8\varphi_{offset}$ held constant. For a concentration of 20 mM $HAuCl_4$, deposition time of 40 min, and deposition area of 3.60 cm^2, the lowest applied potential, $\varphi_{offset} = -0.625$ V, showed no deposition. When the potential was increased to $\varphi_{offset} = -0.8125$ V, rounded plates formed slowly. At $\varphi_{offset} = -1$ V, the plates grew faster and acquired a well-defined geometry with roughly parallel flat faces and edges tracing a regular hexagon shape. At $\varphi_{offset} = -2$ V, dendrites began to grow; Figure 1d shows a typical crystal covering the Au surface around the base of the dendrites, which had roughly μm scale faces and a triangular bipyramid shape with periodic ridges. Figure 1l shows the tips of dendrites grown under the same conditions. Figure 1s shows another variety of the dendrite tip found on the same sample.

The $HAuCl_4$ concentration also influenced the growth of the nanostructures. For a deposition time of 40 min, an area of 3.6 cm^2, and a $\varphi_{offset} = -2$ V, 2 mM $HAuCl_4$ produced spherical granules a few hundred nanometers in diameter (Figure 1e). A concentration of 8 mM produced dendrites with approximately 0.5 μm rounded dendrite tips, and many small granules covering the dendrite stalk (Figure 1f). From 12 to 20 mM, the dendrite surface became smoother, with fewer small granules on the surface, developing the appearance of a single crystal containing periodic ridges running approximately 60° from the direction of growth (Figure 1g−l).

Variation of the time and exposed electrode surface area showed no "loading effect" apparent under SEM inspection—increasing the Coulombs per surface area only increased plate size, and the deposition rate appeared to be constant with time and surface area. Specifically, for the plates grown in 20 mM $HAuCl_4$ at $\varphi_{offset} = -1$ V, 20 min of deposition onto 7.2 cm^2 showed plates of 0.5 μm or less (Figure 1m). A deposition of 20 min onto 3.6 cm^2 showed larger plates, approaching 1 μm in width (Figure 1n). A deposition of 40 min onto 7.2 cm^2 showed similar results (Figure 1o). A deposition of 40 min onto 0.8 cm^2 showed approximately 2 μm width plates (Figure 1p).

Changing the ratio $\varphi_{offset}/\varphi_{pp}$ had little influence on the Au dendrite topography (Figure 1q−t). As such, the ratio $\varphi_{pp} = 8\varphi_{offset}$ was typically held constant.

The shape of Au crystals can provide information on the crystal orientation of the surfaces and can be quantified by measuring the angle between adjacent edges, corners, and branches. For Au plates deposited in 20 mM $HAuCl_4$ at $\varphi_{offset} = -1$ V, the angle between adjacent corners is approximately 60°, producing approximately regular hexagons (Figure 2a). Each corner is the nexus of four edges, two connecting to adjacent corners and two running from the corner to the center of the crystal. The plates are quite flat, with an approximately 100−110° angle between edges connecting corners (Figure 2a) and acute angles between edges that run from the corner to center, such as 23° (Figure 2b). The large plate in Figure 2b shows small recesses between the corners, suggesting growth is primarily at the corners, followed by filling in along the edge between corners. For Au dendrites deposited in 20 mM $HAuCl_4$ at $\varphi_{offset} = -2$ V, the angle between the dendrite branches is 60° (Figure 2c). The angles between adjacent edges is acute, covering a wide range of values from 35 to 80° (Figure 2c,d). The common 60° angle between plate corners and dendrite branches suggests that there is a similar deposition process of preferred growth at the corners, in which a dendrite forms when a corner grows faster than the adjacent edges can fill in. The corner then evolves into a branch, from which new corners can nucleate. As Au has an fcc crystal lattice, the 60° angle between corners indicates a preferred crystallographic growth direction of ⟨110⟩.

DOI: 10.1021/acs.jpcc.8b01831
J. Phys. Chem. C 2018, 122, 10006−10016

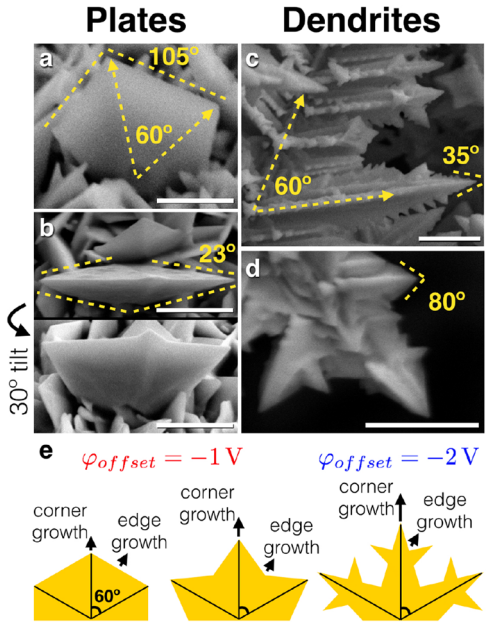

Figure 2. Representative SEMs showing the angle between primary growth directions and the angles between adjacent edges of the Au crystals in (a,b) plates and (c,d) dendrites. (e) Cartoons of the plate growth (left and center) and the dendrite growth (right). Arrows represent the growth velocity of corners and edges. These show how increasing corner growth more than edge growth can give rise to the crystal shapes observed via SEM. Scale bars = 1 μm.

In XRD measurements, the relative intensity of peaks associated with different orientations indicates the relative prevalence of each crystal orientation on the sample surface.[12,13] Figure 3 shows representative patterns for Au

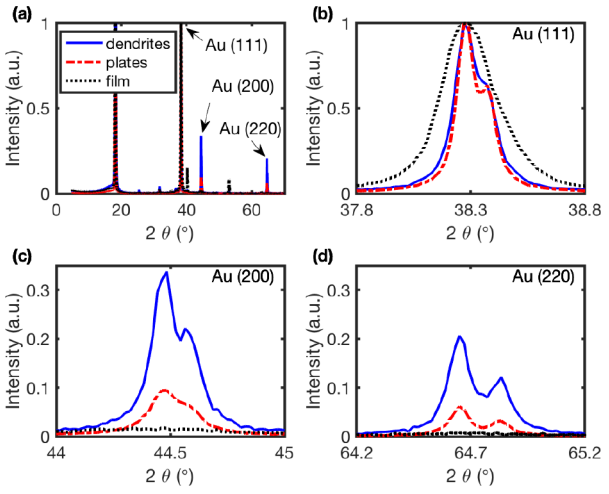

Figure 3. XRD spectrum of Au dendrite, plate, and polycrystalline film samples, normalized so that the Au (111) peak height is 1. (a) Full spectrum, (b) (111) peak, (c) (200) peak, (d) (220) peak.

dendrite, plate, and sputtered film samples, normalized so that the intensity of the {111} peak equals 1. The data for these Au dendrite and plate samples was recorded following 18 h of CO_2 reduction. These data show that all the samples were dominated by {111} surfaces, the dendrites had more surface with {100} and {110} orientations than the plates, and the sputtered film had nearly no {100} or {110} surface. Note, the peaks for the (200) and (220) orientations were considered representative of the {100} and {110} orientations, respectively. The double-peak structure for the curves from Au dendrites and plates indicates that they have high crystallinity, and the single broad {111} peak for the sputtered film indicates that it has lower crystallinity. The two peaks are produced, because the copper source emits two very nearby wavelengths, $K_{\alpha1}$ and $K_{\alpha2}$ at 0.1540 and 0.1544 nm, respectively, which are both reflected by the crystal Bragg planes. Figure S1 shows the XRD patterns for dendrites grown at $\varphi_{offset} = -2$ V for several different φ_{pp}, indicating a slight tendency for more {100} and {110} surface orientation with increasing amplitude.

TEM images allow for spot analysis of surface crystal orientation over small sample areas. Figure 4a shows a dendrite

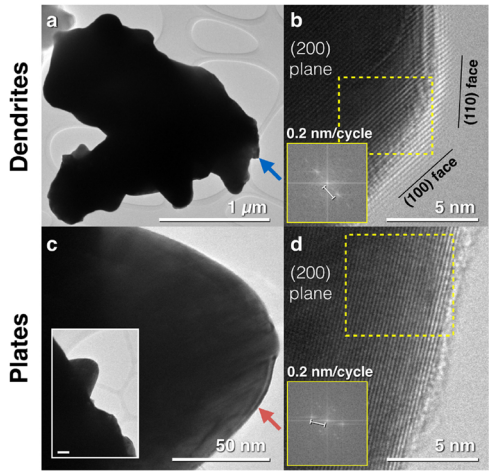

Figure 4. TEM of Au dendrites under (a) low magnification and (b) high magnification; Au plates under (c) low magnification, (d) high magnification. Both scale bars in (c) are 50 nm. Insets in (b) and (d) show the Fourier transform of areas highlighted by dashed line.

crystal, and 4b shows the crystal orientation at a corner of the crystal. The image plane is along the {100} orientation, and the edge appears to terminate in small {100} and {110} faces. Figure 4c shows a plate crystal, and 4d shows the crystal orientation of the flat crystal face. The image plane is also along the {100} orientation, and the edge appears to terminate in a {100} face. No μm scale facets were observed via TEM for either dendrites or plates.

With potentiostatic EIS, we measured the impedance (Z) and phase (ϕ) vs frequency (f) for Au nanostructures made at different φ and in different electrolyte compositions. From this, we calculated the differential capacitance per unit area (C_d/A) of Au electrodes, shown in Figure 5a. From the shape of C_d/A vs φ, we determined the potential of zero charge (PZC) for each electrolyte. Specifically, the curve has a minimum at the PZC in the case of nonspecific binding and dilute electrolyte,[14] as demonstrated for mercury in numerous electrolytes of a concentration of ~10 mM or less.[15] The PZC of Au in vacuum is 0.55 V vs standard hydrogen electrode (V_{SHE}) and should be similar in solutions with low binding energy to the metal surface.[16] We thus considered the local minimum of C_d/A located near 0.55 V_{SHE} to indicate the PZC. For pure $HAuCl_4$ solutions, we modeled our electrode−solution interface with a Randles circuit, shown in Figure S2.[17] From this, we calculated C_d/A of a sputtered Au surface in our standard dendrite growth solution, 20 mM $HAuCl_4$. However, this could only probe φ

DOI: 10.1021/acs.jpcc.8b01831
J. Phys. Chem. C 2018, 122, 10006−10016

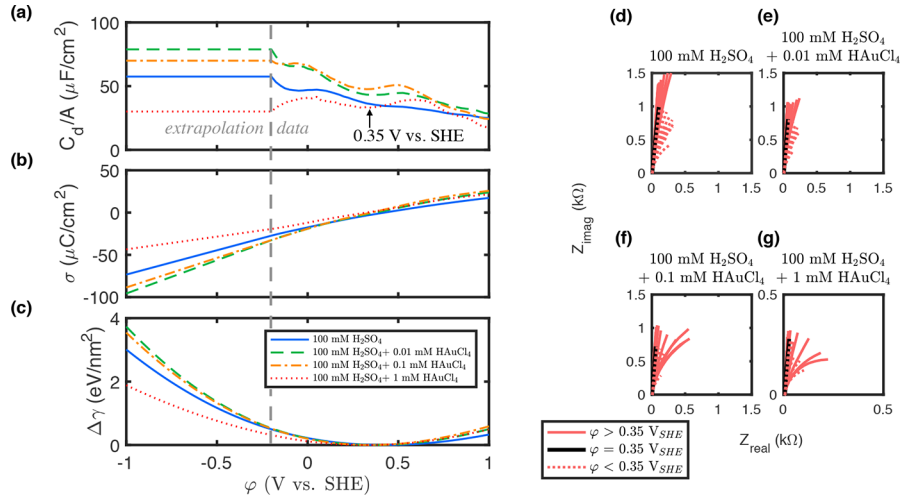

Figure 5. Potentiostatic EIS of a sputtered Au surface with a geometric surface area of 0.8 cm^2 in 100 mM H_2SO_4 with various concentrations of $HAuCl_4$. (a–c) Left of gray dashed line is extrapolation of C_d/A as a constant vs φ, and right of the gray dashed line is measured data. (a) C_d/A vs φ; electrode area, A, was measured by CV of the Au in H_2SO_4. (b) σ vs φ calculated from (a). (c) $\Delta\gamma$ vs φ calculated from (b). (d–g) Nyquist plots of the EIS measurements at each φ, for each of the $HAuCl_4$ concentrations.

near the reduction potential of $AuCl_4^-$, 0.9 V_{SHE} at pH = 1.7, where the reaction kinetics are slow. The overpotential for $AuCl_4^-$ reduction at 0.55 V_{SHE} drives the reaction kinetics faster than $AuCl_4^-$ can diffuse to the electrode surface. This creates a non-negligible Warburg impedance (Z_W) that is convoluted with the capacitive double-layer impedance, evidenced by the deviation from a semicircle in the Nyquist plots in Figure S3 for potentials negative of 0.8 V_{SHE}. The convolution prevents standard analysis of the Randles circuit, which would normally yield C_d and the charge transfer resistance R_{ct}.

Aqueous solutions of pure H_2SO_4 provide a simpler measurement, because no charge transfer reactions should occur in the electrochemical window for water, 0 to 1.23 V_{RHE} (−0.06 to 1.17 V_{SHE} at pH = 1). This allows the system to be modeled as only R_Ω in series with C_d. Figure S4a shows C_d/A vs φ for aqueous solutions of H_2SO_4 of concentrations of 1, 10, 100, and 500 mM. It demonstrates that the minimum in C_d/A near 0.55 V_{SHE} changes little between 1, 10, and 100 mM H_2SO_4, confirming that for this system, 100 mM falls within the "nonspecific binding and dilute electrolyte" case for identifying the PZC. It also shows the PZC to be approximately independent of pH. Nyquist plots in Figure S4d–g show a partial semicircle negative of 0.35 V_{SHE}, which we attribute to a slow transfer of Au from the counter to working electrode. Figures S5–S12 show the individual Nyquist plots. However, for $\omega \gg 1/(C_dR_{ct})$, the imaginary component of the impedance (Z_i) of the Randles circuit reduces from $Z_i = \omega C_d R_{ct}^2/(1 + \omega^2 C_d^2 R_{ct}^2)$ to that of R_Ω and C_d in series, $Z_i = 1/(\omega C_d)$. Figure S13 shows that the measurements of C_d are approximately 50 μF or greater, and the semicircle radii in these plots, representative of R_{ct}, are 200 Ω or greater. As such, the simpler circuit model is valid for $f \gg 100$ Hz, where $f = \omega/2\pi$. Reported C_d values are an average of measurements with $1000 < f < 10\,000$ Hz.

Z_W and R_{ct} are both inversely proportional to the concentration of the species responsible for the Faradaic current.[17] As we are only interested in C_d and not R_{ct}, we used 100 mM H_2SO_4 as a supporting electrolyte and made measurements for 0, 0.01, 0.1, and 1 mM $HAuCl_4$, shown in Figure 5a. With the low $HAuCl_4$ concentrations, R_{ct} in series with Z_W was 200 Ω or greater, as shown by the Nyquist plots in Figure 5d–g. Figures S14–S19 show the individual Nyquist plots. The high total concentration kept the capacitance at 50 μF or greater. As such, for $1000 < f < 10\,000$ Hz, we could again model the system as only R_Ω in series with C_d. This allowed measurement of C_d/A from 1 to −0.2 V_{SHE} in the presence of different $HAuCl_4$ concentrations. Water splitting and significant Au deposition at more negative potentials obscured measurements.

The Lippman, or electrocapillary, equation, shows that $\gamma(\varphi)$ equals the integral of the surface charge density (σ) on the metal half of the metal–electrolyte interface[18]

$$\gamma(\varphi) = \gamma_{PZC} - \int_{PZC}^{\varphi} \sigma(\varphi')\mathrm{d}\varphi' = \gamma_{PZC} - \Delta\gamma(\varphi) \quad (2)$$

where γ_{PZC} is the surface energy at the PZC. To solve this for $\gamma(\varphi)$, we need to know γ_{PZC}, $\sigma(\varphi)$, and the PZC. Per the electrocapillary equation, $\sigma(\varphi)$ can be determined by integrating C_d/A from the PZC to φ

$$\sigma(\varphi) = \int_{PZC}^{\varphi} C_d(\varphi')\mathrm{d}\varphi' \quad (3)$$

By definition, σ(PZC) = 0, which allows evaluation of the integral in eq 3. Figure 5b shows the resulting $\sigma(\varphi)$. From this, the integral in eq 2 can be evaluated for $\Delta\gamma(\varphi)$, shown in Figure 5c. C_d/A was extrapolated as a constant from −0.2 to −1 V_{SHE} to make an approximation of γ down to −1 V_{SHE}. For the two-electrode plate and dendrite depositions, we assumed the Pt counter electrode was at ∼1.5 V_{SHE}: the water oxidation potential of 1.13 V_{SHE} at pH = 1.7 plus several hundred mV of overpotential and ohmic drop. As such, the plate growth would have occurred at $\varphi_{offset} \approx 0.5$ V_{SHE} and dendrite growth at $\varphi_{offset} \approx -0.5$ V_{SHE}. These correspond to decreases in γ of $\Delta\gamma(0.5) \approx 0$ eV/nm^2 and $\Delta\gamma(-0.5) \approx 1$ eV/nm^2. During the deposition half-cycles for plates and dendrites, where $\varphi \approx -3.5$ V_{SHE} and $\varphi \approx -8.5$ V_{SHE}, respectively, our data suggests $\Delta\gamma$ would be many eV/nm^2.

Cyclic voltammetry allowed for measurements of the sample surface area. These were made by sweeping across the oxidation and reduction potentials of Au in H_2SO_4 and integrating the total charge passed during the reduction peak. Assuming a uniform and repeatable Au oxide layer, the relative surface area

DOI: 10.1021/acs.jpcc.8b01831
J. Phys. Chem. C 2018, 122, 10006–10016

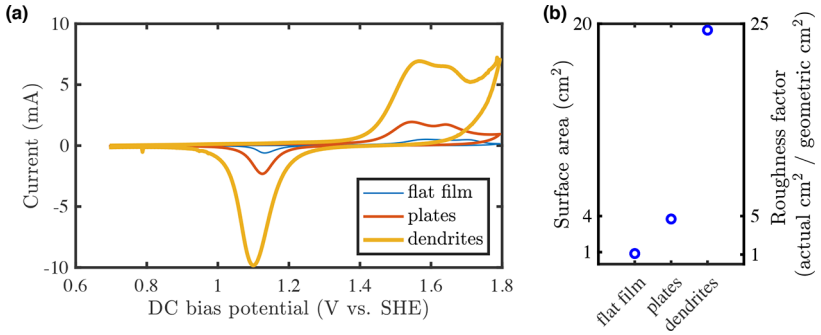

Figure 6. Cyclic voltammetry of dendrites, plates, and a flat film of Au on Si with a geometric area of 0.8 cm^2 in 500 mM sulfuric acid. (a) Overlayed cyclic voltammograms of each nanostructure. (b) Real surface area of the electrode, calculated by integrating the total charge of the Au reduction peak for each curve. The roughness factor was calculated by normalizing relative to the flat film.

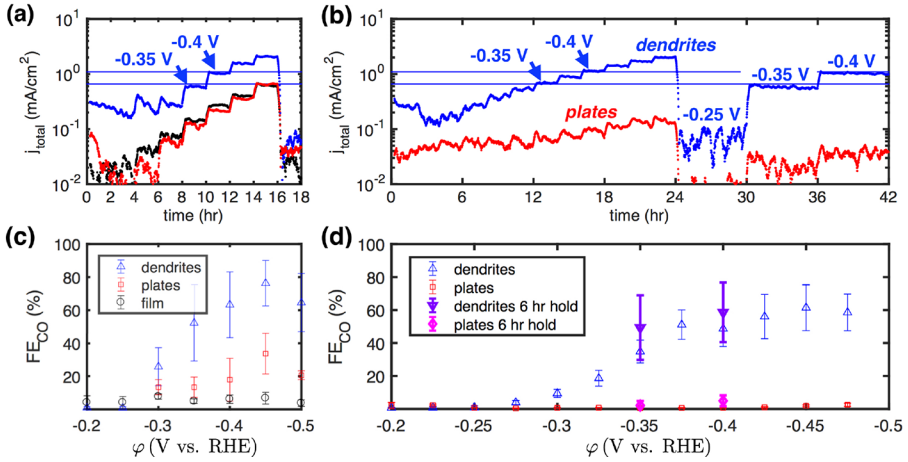

Figure 7. (a) Total current density of a sample with (blue) Au dendrites, (black) Au sputtered film, and (red) Au plates under the potentials of −0.2 to −0.5 V_{RHE}, stepped by −50 mV every 2 h, except for an initial 4 h hold at −0.2 V_{RHE} for the current to stabilize. (b) Total current density of a sample with Au dendrites and plates under the potentials of −0.2 to −0.475 V_{RHE}, stepped by −25 mV every 2 h, and followed by 6 h holds at −0.25, −0.35, and −0.4 V_{RHE} to test stability. (c,d) Faradaic efficiencies for CO vs φ.

of the electrode could be measured.[19] Figure 6a shows the reduction peak of dendrite, plate, and flat Au film samples. Figure 6b shows the actual surface area and the roughness factor of each of these samples, normalized to the flat film. Figure S20 shows data taken between EIS measurements that had different electrolytes. Linear interpolation between these surface area measurements of EIS samples was used to approximate the C_d/A shown in Figure 5a.

CO_2 Electrolysis. XPS measurements before and after CO_2 reduction experiments were used to quantify the surface atomic composition and the Au oxidation state. Figure S21 shows that the XPS spectrum for the Au 4f and O 1s peaks are very similar before and after CO_2 reduction, suggesting that no change is made to the Au oxidation state.

The performance of the Au dendrites, plates, and sputtered film as electrocatalysts for CO_2 reduction was assessed by measuring j_{total} and product gas composition at a variety of applied potentials. Figure 7a shows the geometric j_{total} of the dendrites, plates, and sputtered film; φ was started at −0.2 V_{RHE} for 4 h and then stepped in −50 mV increments every 2 h to −0.5 V_{RHE}. Finally, φ was returned to −0.25 V_{RHE} to test the sample's stability over time. j_{total} at the end of the experiment decreased substantially for the dendrites, but actually increased for the plates and sputtered film. Figure 7b shows the performance of dendrite and plate samples starting at −0.2 V_{RHE} and stepping in −25 mV increments every 2 h to −0.475 V_{RHE}, followed by 6 h holds at −0.25, − 0.35, and −0.4 V_{RHE}. With a smaller step size, more time will have passed before each electric potential is reached. The two different potential step sizes were compared to ensure that this did not affect catalytic performance, a confirmation that the catalysts did not degrade significantly with time. For both dendrites and plates, this hold to test stability showed a much lower j_{total} at −0.25 V_{RHE} than the start of the experiment, but −0.35 and −0.4 V_{RHE} showed only slight degradation. Comparing the −50 mV steps to the −25 mV steps, j_{total} was found to match very well at −0.35 and −0.4 V_{RHE}. The −0.25 V_{RHE} current densities matched for the end-of-experiment holds. For both step increments, the dendrite samples showed a decreasing j_{total} at each applied potential until −0.35 V_{RHE} was applied, after which j_{total} was stable with time for increasingly negative φ. The plates showed a similar response for the −50 mV step but continued to show decreasing j_{total} at all applied potentials throughout the −25 mV steps.

The Faradaic efficiencies for production of CO by the dendrites, plates, and sputtered films are shown in Figure 7c for the −50 mV steps and in 7d for the −25 mV steps. The data show dendrites have approximately 50−60% Faradaic efficiency for CO for $\varphi \leq -0.35$ V_{RHE}. The plates and film have a CO Faradaic efficiency of approximately 20−40% and 5−10%, respectively, during the −50 mV steps; plates showed a nearly 0% CO Faradaic efficiency during −25 mV steps. Notably, the

DOI: 10.1021/acs.jpcc.8b01831
J. Phys. Chem. C 2018, 122, 10006−10016

dendrites seemed to show a slight increase in the CO Faradaic efficiency during the 6 h holds at −0.35 and −0.4 V_{RHE}, compared to the values measured during the 2 h 25 mV steps; the CO Faradaic efficiency for the 6 h hold at −0.25 V_{RHE} was too noisy to produce a reliable average. Figure 8 shows Tafel

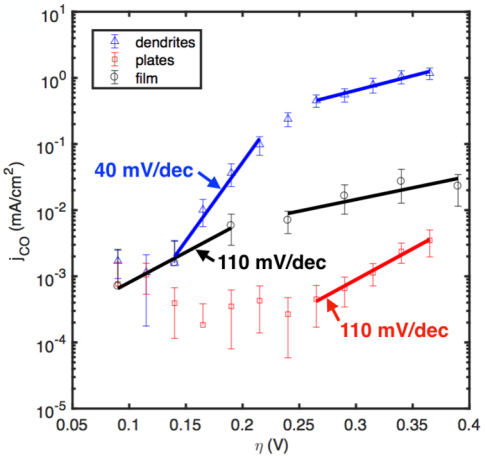

Figure 8. Tafel slopes of Au dendrite and Au plate samples from −25 mV steps, and Au sputtered film from −50 mV steps.

plots for the dendrites, plates, and sputtered film. The data show the kinetically limited reaction regimes to have a slope of 40 mV/dec for dendrites and 110 mV/dec for the plates and film.

DISCUSSION

During electrocrystallization, the solute near the crystal surface gets added to the crystal surface via an electrochemical reaction. This depletes the solute concentration, establishing a diffusion boundary layer. In continued crystallization, the solute must diffuse across the diffusion boundary layer from the solution bulk to the crystal surface. The slower of these serial steps, diffusion or electrochemical reaction, will determine the rate of deposition and control the morphology of the crystals grown. Equivalent steps occur for crystallization from melts and vapors.

When crystallization is diffusion limited, three-dimensional structures can be formed, such as dendrites. This occurs, because protrusions on the crystal surface extend into the diffusion field, receiving faster diffusion of solute than the surrounding flat surface. The phenomenon is known as the Mullins−Sekerka effect.[20] The sharper the protrusions, the faster solute diffusion will be. This effect is balanced by the Gibbs−Thomson effect,[21] in which the local surface energy of a crystal increases with decreasing radius of curvature; for a given deposition condition, protrusions with radius of curvature below a certain value will be thermodynamically unstable and dissolve/melt/sublimate.

To provide a model that describes the morphology of the crystals, we draw comparisons between the electrocrystallization and crystallization from melts and vapors. For crystallization upon a polycrystalline film, where a random assortment of crystal orientations are present for nucleation, growth will proceed along the orientation of lowest surface stiffness, γ^*.[22] This is a measure of the energy per unit area necessary to create curvature on a surface; adding atoms onto an atomically flat surface requires creating such a curvature. γ^* is derived from the surface energy, γ, via Herring's Equation;[23,24] γ is defined as the energy it takes to create a unit area of interface between the crystal and solution. Figure 9a shows the predicted values of γ for several ambient phases and crystal orientations. Comparison of molecular dynamics simulations and experiments[22,25,26] has developed a theory to describe the dendrite morphology of different metals solidified from their melts. These calculations approximate the surface energy of crystals with underlying cubic symmetry by expansion into a series of cubic harmonics with two anisotropy factors, ϵ_1 and ϵ_2

$$\gamma(\theta, \phi) = \gamma_0[1 + \epsilon_1 K_1(\theta, \phi) + \epsilon_2 K_2(\theta, \phi) + ...] \quad (4)$$

where the cubic harmonics are combinations of the standard spherical harmonics with cubic symmetry. The particular K_1 and K_2 referenced above are

$$K_1(\theta, \phi) = \sum_{i=1}^{3} n_i^4 - \frac{3}{5} \quad (5a)$$

$$K_2(\theta, \phi) = 3\sum_{i=1}^{3} n_i^4 + 66 n_1^2 n_2^2 n_3^2 - \frac{17}{7} \quad (5b)$$

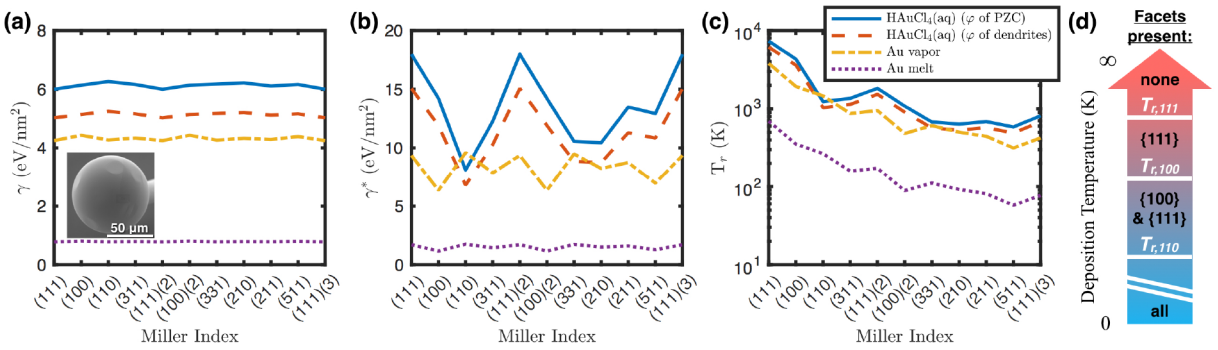

Figure 9. Comparison of the tendency of Au to form facets at various Miller indices, in several ambient phases. Experimental d_{hkl} values from [ref 27]. To calculate T_r, γ^* was assumed constant with temperature. For an Au vapor ambient phase, we used $\gamma_0 \approx 6.16$ (eV/nm^2), the value for Au in a noninteracting atmosphere.[16] For an Au-melt ambient phase, $\gamma_{0,melt} = 0.786$ (eV/nm^2) [ref 25]. For the Au vapor and Au melt, we used $\epsilon_1 = 0.064 \pm 0.011$ and $\epsilon_2 = 0.003 \pm 0.002$ [ref 26]. For the HAuCl$_4$(aq) ambient phase, we used $\gamma_0 \approx 6.16$ (eV/nm^2) for the PZC and $\gamma_0 \approx 5.16$ (eV/nm^2) for the dendrite φ_{offset}, consistent with $\Delta\gamma$ measurements in 1 mM HAuCl$_4$(aq) + 100 mM H$_2$SO$_4$(aq). (a) γ; the inset shows a rounded Au sphere with {111} facets formed by melting an Au wire. (b) γ^*. (c) T_r. (d) Cartoon of facets present at different deposition temperatures, relative to T_r for each Miller index.

DOI: 10.1021/acs.jpcc.8b01831
J. Phys. Chem. C 2018, 122, 10006−10016

where $\hat{n} = (n_1, n_2, n_3)$ is the interface normal. In spherical coordinates, these have their standard definition, $n_1 = \cos(\phi)\sin(\theta)$, $n_2 = \sin(\phi)\sin(\theta)$, $n_3 = \cos(\theta)$. Eq 4 shows that the shape of γ is dictated by the value of ϵ_1 and ϵ_2, scaled in magnitude by the surface energy prefactor, γ_0. ϵ_1 and ϵ_2 thus determine the shape of γ^* and the direction of growth of dendritic crystals. This angular dependence of the surface stiffness tensor can be calculated by

$$\gamma^* = 2\gamma + \frac{\partial^2\gamma}{\partial\theta^2} + \frac{1}{\sin^2(\theta)}\frac{\partial^2\gamma}{\partial\phi^2} + \cot(\theta)\frac{\partial\gamma}{\partial\theta} \quad (6)$$

Values of ϵ_1 and ϵ_2 for various metals solidifying from their melt have been calculated by these molecular dynamics simulations, with plots generated of the inverse of γ^* and the expected dendrite morphology.[22] Through comparison of these with the dendrite morphology shown in Figure 2, the single branch in each ⟨110⟩ direction suggests that the anisotropy factors for Au electrocrystallization from $HAuCl_4$(aq) are approximately $\epsilon_1 = 0.02$ and $\epsilon_2 = -0.02$. Interestingly, this differs significantly from the values reported for Au dendrites grown from their melt, where $\epsilon_1 = 0.064 \pm 0.011$ and $\epsilon_2 = -0.003 \pm 0.002$,[26] corresponding to dendrite growth in the ⟨100⟩ directions. As such, electrocrystallization allows for a unique dendritic Au structure than crystallization from melts allows. Figure 9b shows γ^* for several ambient phases. Electrocrystallization of Au dendrites with different growth directions would require tuning the anisotropy parameters, potentially possible with chemicals that would selectively interact with certain Au crystallographic orientations.

It has been shown through comparison of experiment and density functional theory calculations that γ of the Au {111} surface in vacuum is approximately 6 eV/nm^2.[16] With use of the ϵ_1 and ϵ_2 values determined above for electrocrystallization, this corresponds to $\gamma_0 = 6.16$ eV/nm^2. This is a rough estimate; other work has reported $\gamma_0 = 4.3$ (eV/nm^2).[28] Using a model that considers only polarization due to the ionic double layer, calculations showed γ to be unchanged by immersion in 500 mM H_2SO_4(aq). This model calculated the PZC to be 0.55 V_{SHE}.

Our measurements show the PZC of Au in 1, 10, and 100 mM H_2SO_4(aq) to be ∼0.35 V_{SHE}—and closer to ∼0.4 V_{SHE} for 500 mM. This suggests that there is some interaction between the Au and H_2SO_4(aq) besides polarization. The negative shift indicates a negative species in the H_2SO_4(aq) with an affinity to the Au, which at 0.55 V_{SHE} would draw a net positive charge onto the Au. The PZC of Au in 0.01, 0.1, and 1 mM $HAuCl_4$(aq) + 100 mM H_2SO_4(aq) is also 0.35 V_{SHE}. If we assume $\Delta\gamma(0.55) = 0.1$ eV/nm^2 equals the change in γ from the interactions with solution, then the change is negligible compared to γ_0(PZC) ≈ 6 eV/nm^2. Figure 5c does show a significant change of 1 eV/nm^2 at $\varphi = -0.5$ V_{SHE}, though. This roughly corresponds to $\varphi_{offset} = -2$ V for dendrite deposition. Under our approximations, γ would reach 0 eV/nm^2 before the deposition half-cycle potentials for plate and dendrite growth, −3.5 and −8.5 V_{SHE}, respectively. A negative γ would correspond to a dissolving electrode, so our approximation that C_d/A is constant at potentials negative of −0.2 V_{SHE} is evidently an overestimate. γ is likely quite low at these very negative potentials, though.

Regarding the structure of the crystal's surface, the surface of a crystal is either a flat atomically smooth facet with a particular crystallographic orientation or a rounded atomically rough surface with a gradually changing orientation along its surface. If the deposition temperature is above the roughening temperature (T_r) for a particular crystallographic orientation, then the surface will be rough. T_r is a function of γ^* for a given ambient growth phase[29]

$$kT_{r,hkl} = \frac{2}{\pi}\gamma^*(T_r)d_{hkl}^2 \quad (7)$$

where d_{hkl} is the interplanar distance parallel to the crystal face. "The more closely packed a given crystal face is, the larger the interplanar distance, and the higher T_r will be."[24] For example, on an fcc lattice, the most closely packed face has $d_{111} = a_0/\sqrt{3} \approx 0.6a_0$, followed by $d_{100} = a_0/2 = 0.5a_0$; deposition at a temperature of $T_{r,100} < T < T_{r,111}$ should produce crystals with rough rounded surfaces except for flat {111} facets. Figure 9c shows T_r for several ambient phases. Figure 9d demonstrates the meaning of T_r via a cartoon. The Au surface should be completely rough for room temperature deposition at φ, for which $\gamma_0 \leq 0.25$ eV/nm^2.

For context, we first consider T_r in Figure 9c for an Au surface in an Au melt and Au vapor. The plot indicates that solidification from an Au melt should not produce faceted Au crystals, as $T_r = 700$ K for the most densely packed faces, {111}, is below the melting point of 1300 K.[26] This is approximately confirmed by the SEM in the Figure 9a inset, showing the result of melting the tip of an Au wire with a butane flame and letting it crystallize in room temperature atmosphere; all of the surfaces appear rounded except for small facets in the {111} directions. For the Au vapor, lacking a better option, ϵ_1 and ϵ_2 were somewhat arbitrarily set to the same values as for an Au melt. $T_r = 5400$ K for growth from an Au vapor, much higher than for the melt. However, Au must be raised over 900 K just to reach the minute vapor pressure of 10^{-11} Torr and over 1500 K to reach 10⁻3 Torr.[30] As such, Au vapor should produce faceted Au crystals but would require low pressure and high temperature equipment.

Per Figure 9c, T_r for $HAuCl_4$(aq) at the PZC and the dendrite φ_{offset} is slightly larger than for an Au vapor and has a different shape than the melt and vapor due to the different ϵ_1 and ϵ_2 values. The large T_r means that, for deposition at room temperature and near the PZC, many crystallographic orientations should have faceted surfaces rather than rough. Since the {111} facet has the lowest surface energy, this would be expected to dominate, assuming local thermodynamic equilibrium during crystal growth. This is consistent with our XRD analysis of plates, which shows {111} to dominate. T_r for the dendrite φ_{offset} potential is slightly lower but still over 500 K for all Miller indices considered. XRD does show {111} to continue to dominate the dendrites, but the peaks for {100} and {110} increase significantly compared to the plates. Growth of these crystals is diffusion limited, which could prevent full formation of {111} facets and explain these increased peaks. Observations in TEM show nm scale {100} and {110} facets along rounded surfaces; no {111} were observed. The prevalence of rough surfaces with scattered small facets, as observed via TEM, suggests that T_r for an Au surface may depend on the instantaneous potential. For our deposition process, this would sweep T_r widely between 0 and over 500 K during the MHz potential oscillation.

The structure of the Au plates is very similar to several Au[12,31,32] and Ag[33−35] plates recently reported. In these reports, it is proposed that sufficiently low ion concentration ensures that nuclei cannot grow autocatalytically into lower-energy

DOI: 10.1021/acs.jpcc.8b01831
J. Phys. Chem. C 2018, 122, 10006−10016

polyhedral structures. Instead, stacking faults and/or twin defects at the particle edges provide favorable sites for nucleation of new atomic layers on the {111} facets. The similarity in structure and dilute electrolyte suggests that a similar kinetically limited growth mechanism is responsible for the morphology of the Au plates we produced.

The formation of dendrites at more cathodic φ is consistent with the mechanism discussed above. The higher overpotential could be sufficient to drive the kinetics of deposition faster than solute diffusion, establishing the diffusion limited growth condition. Separately, this overpotential may also drive nucleation of new atomic layers without the aid of twin defects and thereby change the crystal morphology.

The effect of an MHz potential oscillation on dendrite growth has been described in detail.[7−11] The primary result of the oscillation is to increase the effective solute concentration at the dendrite surface, since the solute can replenish during the anodic half of the oscillation. The solute concentration has a significant impact on the dendrite morphology; as the concentration increases, we have shown the dendrite crystals have fewer small granules on them (Figure 1e−l), and literature has shown that the tip gets sharper.[5,10] However, increasing the concentration of $HAuCl_4$ has the simultaneous impact of lowering the pH. Lower solution pH is understood to produce rounded surfaces instead of faceted ones.[36]

Regarding CO_2 reduction electrocatalyst efficacy, the dendrites had the highest current density, while that of the plates and sputtered film was similar. Dendrites also showed the highest selectivity for CO, followed by the plates, and finally the sputtered film. This selectivity is consistent with the literature. Calculations and experiments have demonstrated the binding energy of the intermediate COOH to have the relative magnitudes of {110} > {100} > {111}.[37] This intermediate should thus be most stable on the dendrites, which have the greatest proportion of {110} and {100} facets, followed by plates, and finally the sputtered film.

The mechanism of the conversion of CO_2 to CO at a gold catalyst in an aqueous bicarbonate solution involves two electron transfers and two proton transfers to a CO_2. Different mechanisms for this process have been proposed, as summarized recently.[2] In all mechanisms, if the first reaction step produces an intermediate that is not stable on the Au surface, then it will be the rate limiting step (RLS). If the intermediate is stable, then the RLS will be the last step that produces an unstable (i.e., poorly bound) species. We assume the symmetry factor $\beta = 0.5$ for the electron transfers. As such, the 40 mV/dec slope measured for the dendrites suggests the RLS is an electron transfer to the intermediate COOH, producing CO and H_2O. This step completes the reaction and is thus the lowest possible Tafel slope for mechanisms that are consistent with the appearance of a 40 mV/dec slope. The 110 mV/dec slope measured for the plates and film matches the first or second reaction step of the mechanisms reported in the above-mentioned article. Scheme 1 shows two example schemes, in which the first step involves an electron transfer with a predicted Tafel slope of 118 mV/dec, and the last step is an electron transfer with a predicted Tafel slope of 40 mV/dec Scheme 1a depicts an electron transfer to bind the CO_2 to Au, followed by protonation, and finally a proton-coupled electron transfer (PCET). Scheme 1b depicts a PCET step to bind the CO_2 to Au, followed by another PCET to finish the reaction. The H^+ in the scheme cartoon represents a generic proton source—further studies of the reaction orders of different chemical species would be necessary to determine the proton source. The 40 mV/dec slope has only been produced by one other structure of which we were aware, Au nanoneedles.[5,6]

Scheme 1. Two Possible Reaction Schemes for the CO_2RR on Au Plates and Dendrites[a]

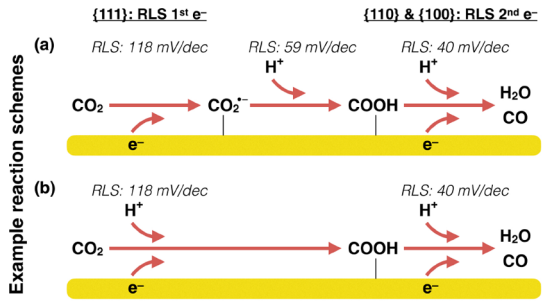

[a](a) An electron transfer, followed by protonation, and finally a PCET. (b) Two sequential PCET reactions. The H^+ represents any proton source. The predicted Tafel slope for the first electron transfer matches measurements of {111} dominated plates; the predicted Tafel slope for the second electron transfer matches measurements of {110} and {100}-rich dendrites.

The dendrites clearly have a much higher specific surface area than the film or plates, which can in part explain their higher current density. However, other characteristics are independent of the specific surface area. The lower Tafel slope of the dendrites is evidence of higher CO_2RR activity, which can result from stronger binding to the intermediate COOH. This reaffirms the expectation that nanostructures with a greater proportion of {110} and {100} relative to {111} facets provide faster reaction kinetics.

The potential −0.35 V_{RHE} stands out as a turning point where catalytic performance significantly increases as the potential becomes more negative. This was true for the dendrites, plates, and film. At the more negative potentials, $j_{total}(t)$ is stable during 42 h of CO_2RR and shows a stark decrease in noise. The dendrites show a somewhat abrupt increase in the CO Faradaic efficiency from ∼0 to ∼50% with increasing overpotentials. Finally, the Tafel slopes change: for both of the dendrites and the film there is an increase in the mV/dec of partial current density, typically understood to signify the point at which the reaction kinetics outpace the rate of mass transport to make the reaction mass transport limited. For plates, the slope decreases from ∞ to 110 mV/dec at this potential. Notably, a slight increase in the CO Faradaic efficiency is observed during the 6 h potential holds, as shown in Figure 7d.

The plate samples demonstrated inconsistent results between −25 mV steps and −50 mV steps. This may be a result of poor stability of the plates during the long experiment time of the −25 mV steps, resulting in degradation. We excluded the CO Faradaic efficiency at −0.2 and −0.25 V_{RHE} during −50 mV steps, because it was produced at very low and unstable current density, giving the data questionable accuracy.

CONCLUSIONS

In summary, electrocrystallization with an MHz oscillation of the potential φ allows for the fabrication of various Au nanostructures, namely, plates and dendrites. According to XRD analysis, the surface of dendrites contains a larger proportion of {100} and {110} than the plates; the other major surface orientation on both nanostructures is {111}. EIS

DOI: 10.1021/acs.jpcc.8b01831
J. Phys. Chem. C 2018, 122, 10006−10016

measurements of C_d/A vs φ for polycrystalline Au in aqueous solutions show the PZC $\approx$ 0.35 V_{SHE}, with γ decreasing as φ moves away from the PZC. Adaptation of a model for crystallization from melts and vapors suggests that, in this electrocrystallization, more crystal orientations should be faceted at φ with large γ. No facets should be present for room temperature deposition at φ with $\gamma_0 \leq 0.25$ eV/nm^2. Comparison with literature on crystallization from aqueous solutions suggests that plate growth is kinetically limited, growing via stacking faults and/or twin defects at the plate edges to produce predominantly {111} surfaces. Dendrite growth is likely mass transport limited, creating hierarchical nanostructures that are ~10 μm tall. SEMs of plate corners and dendrite tips look similar, suggesting that the kinetic process for the growth at these sites may be the same. Due to the hierarchical nature of these nanostructures, with nm scale features on μm scale plates and dendrites, there is a certain degree of randomness and variation of Au surface within each sample. As such, precise control of exposed facets proves to be challenging. The averaging effect of XRD over cm^2 areas made it a powerful tool for analyzing the surface's distribution of crystal orientation. The different nanostructures were found to have significantly different performance as CO_2RR electrocatalysts, supporting previous findings that {100} and {110} orientations are more active for CO_2RR than the {111} orientation. Stable performance was observed for 42 h on the dendrites. φ = −0.35 V_{RHE} was observed to be the turn-on potential for the CO_2RR; cathodic of this potential $j_{total}(t)$ was more stable, and the dendrite's Faradaic efficiency for CO was ~50%. For future studies, higher $HAuCl_4$ concentrations may be considered to change the kinetic process, which for plates was likely dependent on low ion concentration. To avoid {111} surfaces, which our data suggests have the highest roughening temperature, two approaches could be taken. First, more cathodic φ could be considered as a means to avoid the formation of any facets. Second, φ near the PZC could be focused on, as a means to maximize the formation of facets besides {111}.

■ ASSOCIATED CONTENT

Supporting Information

The Supporting Information is available free of charge on the ACS Publications website at DOI: 10.1021/acs.jpcc.8b01831.

Circuit model schematics for electrochemical impedance spectroscopy (EIS) measurements; Nyquist plots used to calculate the differential capacitance of an Au surface; XRD spectra that show little change of facet preference between Au nanostructures deposited using different voltage amplitudes; differential capacitance, surface charge, and change in surface energy of an Au surface in different concentrations of sulfuric acid to establish an understanding of how an Au surface interacts with sulfuric acid—the supporting electrolyte used to study the interactions between an Au surface and chloroauric acid; electrochemical surface area measurements of the Au surface during EIS measurements; XPS spectra of the Au nanostructured surface before and after CO_2 reduction experiments (PDF)

■ AUTHOR INFORMATION

Corresponding Authors

*E-mail: nathan.nesbitt@gmail.com; Phone: +1-617-552-3595 (N.T.N.)
*E-mail: w.smith@tudelft.nl; Phone: +31-15-27-82659 (W.A.S.)
*E-mail: naughton@bc.edu; Phone: +1-617-552-3575 (M.J.N.)

ORCID

Nathan T. Nesbitt: 0000-0002-1806-1077
Samantha Jaszewski: 0000-0002-4958-1219
Fazel Tafti: 0000-0002-5723-4604
Michael J. Burns: 0000-0001-9804-405X
Wilson A. Smith: 0000-0001-7757-5281
Michael J. Naughton: 0000-0002-6733-2398

Notes

The authors declare no competing financial interest.

■ ACKNOWLEDGMENTS

This work was financially supported by the National Science Foundation Graduate Research Fellowship under Grant No. DGE-1258923, including support through the Global Research Opportunities Worldwide program. Any opinion, findings, and conclusions or recommendations expressed in this material are those of the authors(s) and do not necessarily reflect the views of the National Science Foundation.

■ REFERENCES

(1) Hori, Y. Electrochemical CO_2 reduction on metal electrodes. *Mod. Aspect. Electroc.* **2008**, *42*, 89−189.
(2) Wuttig, A.; Yoon, Y.; Ryu, J.; Surendranath, Y. Bicarbonate is not a general acid in Au-catalyzed CO_2 electroreduction. *J. Am. Chem. Soc.* **2017**, *139*, 17109−17113.
(3) Vermaas, D. A.; Sassenburg, M.; Smith, W. A. Photo-assisted water splitting with bipolar membrane induced pH gradients for practical solar fuel devices. *J. Mater. Chem. A* **2015**, *3*, 19556−19562.
(4) Chen, Y.; Li, C. W.; Kanan, M. W. Aqueous CO_2 reduction at very low overpotential on oxide-derived Au nanoparticles. *J. Am. Chem. Soc.* **2012**, *134*, 19969−19972.
(5) Liu, M.; Pang, Y.; Zhang, B.; De Luna, P.; Voznyy, O.; Xu, J.; Zheng, X.; Dinh, C. T.; Fan, F.; Cao, C.; et al. Enhanced electrocatalytic CO_2 reduction via field-induced reagent concentration. *Nature* **2016**, *537*, 382−386.
(6) Saberi Safaei, T.; Mepham, A.; Zheng, X.; Pang, Y.; Dinh, C.-T.; Liu, M.; Sinton, D.; Kelley, S. O.; Sargent, E. H. High-density nanosharp microstructures enable efficient CO_2 electroreduction. *Nano Lett.* **2016**, *16*, 7224−7228.
(7) Cheng, C.; Gonela, R. K.; Gu, Q.; Haynie, D. T. Self-assembly of metallic nanowires from aqueous solution. *Nano Lett.* **2005**, *5*, 175−178.
(8) Talukdar, I.; Ozturk, B.; Flanders, B. N.; Mishima, T. D. Directed growth of single-crystal indium wires. *Appl. Phys. Lett.* **2006**, *88*, 221907.
(9) Ozturk, B.; Flanders, B. N.; Grischkowsky, D. R.; Mishima, T. D. Single-step growth and low resistance interconnecting of gold nanowires. *Nanotechnology* **2007**, *18*, 175707.
(10) Ozturk, B.; Talukdar, I.; Flanders, B. N. Directed growth of diameter-tunable nanowires. *Nanotechnology* **2007**, *18*, 365302.
(11) Flanders, B. N. Directed electrochemical nanowire assembly: Precise nanostructure assembly via dendritic solidification. *Mod. Phys. Lett. B* **2012**, *26*, 1130001.
(12) Guo, S.; Wang, L.; Wang, E. Templateless, surfactantless, simple electrochemical route to rapid synthesis of diameter-controlled 3D flowerlike gold microstructure with "clean" surface. *Chem. Commun.* **2007**, 3163−3165.

DOI: 10.1021/acs.jpcc.8b01831
J. Phys. Chem. C 2018, 122, 10006−10016

(13) Sun, Y.; Xia, Y. Shape-controlled synthesis of gold and silver nanoparticles. *Science* **2002**, *298*, 2176−2179.
(14) Parsons, R. Electrical double layer: Recent experimental and theoretical developments. *Chem. Rev.* **1990**, *90*, 813−826.
(15) Grahame, D. C. The electrical double layer and the theory of electrocapillarity. *Chem. Rev.* **1947**, *41*, 441−501.
(16) Zhuang, H.; Tkalych, A. J.; Carter, E. A. Surface energy as a descriptor of catalytic activity. *J. Phys. Chem. C* **2016**, *120*, 23698−23706.
(17) Bard, A. J.; Faulkner, L. R. *Electrochemical Methods: Fundamentals and Applications*, 2nd ed.; John Wiley & Sons, Inc.: New York, 2001.
(18) Giesen, M.; Beltramo, G.; Dieluweit, S.; Müller, J.; Ibach, H.; Schmickler, W. The thermodynamics of electrochemical annealing. *Surf. Sci.* **2005**, *595*, 127−137.
(19) Jia, F.; Yu, C.; Ai, Z.; Zhang, L. Fabrication of nanoporous gold film electrodes with ultrahigh surface area and electrochemical activity. *Chem. Mater.* **2007**, *19*, 3648−3653.
(20) Mullins, W. W.; Sekerka, R. F. Stability of a planar interface during solidification of a dilute binary alloy. *J. Appl. Phys.* **1964**, *35*, 444−451.
(21) Kessler, D. A.; Koplik, J.; Levine, H. Pattern selection in fingered growth phenomena. *Adv. Phys.* **1988**, *37*, 255−339.
(22) Haxhimali, T.; Karma, A.; Gonzales, F.; Rappaz, M. Orientation selection in dendritic evolution. *Nat. Mater.* **2006**, *5*, 660−664.
(23) Herring, C. The Use of Classical Macroscopic Concepts in Surface-Energy Problems. In *Structure and Properties of Solid Surfaces*; Gomer, R., Smith, C. S., Eds.; University of Chicago Press: Chicago, 1953; Chapter 1, pp 5−81.
(24) Markov, I. V. *Crystal Growth for Beginners: Fundamentals of Nucleation, Crystal Growth and Epitaxy*, 3rd ed.; World Scientific Publishing: Singapore, 2017.
(25) Hoyt, J. J.; Asta, M. Atomistic computation of liquid diffusivity, solid-liquid interfacial free energy, and kinetic coefficient in Au and Ag. *Phys. Rev. B: Condens. Matter Mater. Phys.* **2002**, *65*, 214106.
(26) Hoyt, J. J.; Asta, M.; Karma, A. Atomistic and continuum modeling of dendritic solidification. *Mater. Sci. Eng., R* **2003**, *41*, 121−163.
(27) Davey, W. P. Precision measurements of the lattice constants of twelve common metals. *Phys. Rev.* **1925**, *25*, 753−761.
(28) Barmparis, G. D.; Remediakis, I. N. First-principles atomistic Wulff constructions for gold nanoparticles. 2012, arXiv:1111.4667. arXiv.org e-Print archive. https://arxiv.org/abs/1111.4667.
(29) Fisher, D. S.; Weeks, J. D. Shape of crystals at low temperatures: Absence of quantum roughening. *Phys. Rev. Lett.* **1983**, *50*, 1077−1080.
(30) American Welding Society. *Brazing Manual, 3rd ed.*; American Welding Society: Miami, 1975.
(31) Zhu, M.; Lei, B.; Ren, F.; Chen, P.; Shen, Y.; Guan, B.; Du, Y.; Li, T.; Liu, M. Branched Au nanostructures enriched with a uniform facet: Facile synthesis and catalytic performances. *Sci. Rep.* **2015**, *4*, 5259.
(32) Sun, X.; Dong, S.; Wang, E. Large-scale synthesis of micrometer-scale single-crystalline Au plates of nanometer thickness by a wet-chemical route. *Angew. Chem.* **2004**, *116*, 6520−6523.
(33) Xiong, Y.; Siekkinen, A. R.; Wang, J.; Yin, Y.; Kim, M. J.; Xia, Y. Synthesis of silver nanoplates at high yields by slowing down the polyol reduction of silver nitrate with polyacrylamide. *J. Mater. Chem.* **2007**, *17*, 2600−2602.
(34) Xia, Y.; Xiong, Y.; Lim, B.; Skrabalak, S. E. Shape-controlled synthesis of metal nanocrystals: Simple chemistry meets complex physics? *Angew. Chem., Int. Ed.* **2009**, *48*, 60−103.
(35) Tang, S.; Meng, X.; Wang, C.; Cao, Z. Flowerlike Ag microparticles with novel nanostructure synthesized by an electrochemical approach. *Mater. Chem. Phys.* **2009**, *114*, 842−847.
(36) Budevski, E.; Staikov, G.; Lorenz, W. J. *Electrochemical Phase Formation and Growth*; Wiley-VCH, 1996.
(37) Back, S.; Yeom, M. S.; Jung, Y. Active sites of Au and Ag nanoparticle catalysts for CO_2 electroreduction to CO. *ACS Catal.* **2015**, *5*, 5089−5096.

DOI: 10.1021/acs.jpcc.8b01831
J. Phys. Chem. C 2018, 122, 10006−10016

Au Dendrite Electrocatalysts for CO_2 Electrolysis

Nathan T. Nesbitt,[*,†] Ming Ma,[‡] Bartek J. Trześniewski,[‡] Samantha Jaszewski,[†] Fazel Tafti,[†] Michael J. Burns,[†] Wilson A. Smith,[*,‡] and Michael J. Naughton[*,†]

†*Department of Physics, Boston College, Chestnut Hill, Massachusetts 02467, United States*

‡*Materials for Energy Conversion and Storage (MECS), Department of Chemical Engineering, Faculty of Applied Sciences, Delft University of Technology, 2629 HZ Delft, The Netherlands*

E-mail: nathan.nesbitt@gmail.com; w.smith@tudelft.nl; naughton@bc.edu

Phone: +1-617-552-3595; +31-15-27-82659; +1-617-552-3575

Supporting Information

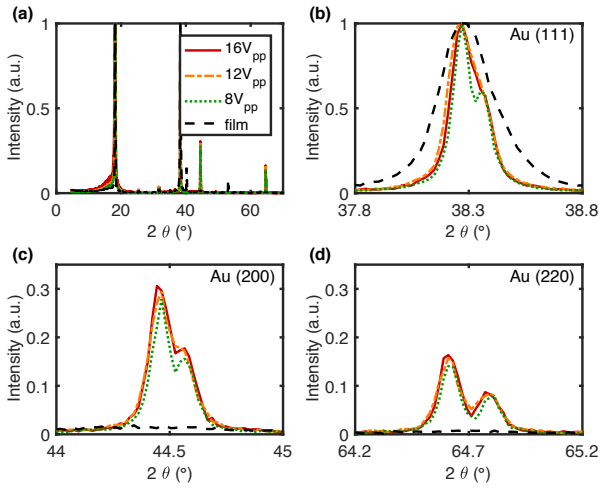

Figure S1: XRD spectrum of Au dendrites grown at $\varphi_{\text{offset}} = -2$ V with different potential amplitudes, normalized so the Au (111) peak height is 1. (a) full spectrum, (b) (111) peak, (c) (200) peak, (d) (220) peak.

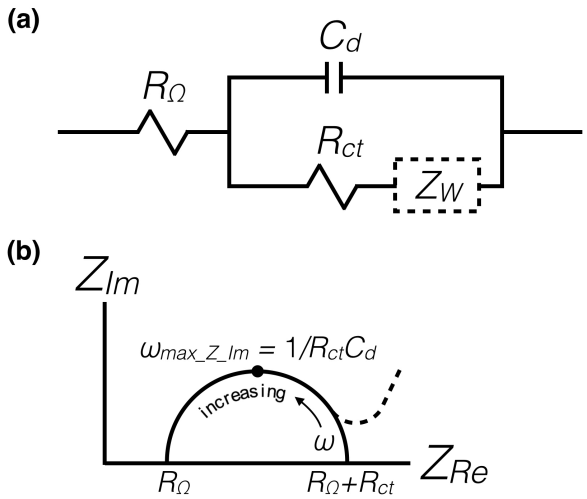

Figure S2: Randles circuit model with ideal EIS response, used to interpret EIS data.[1]

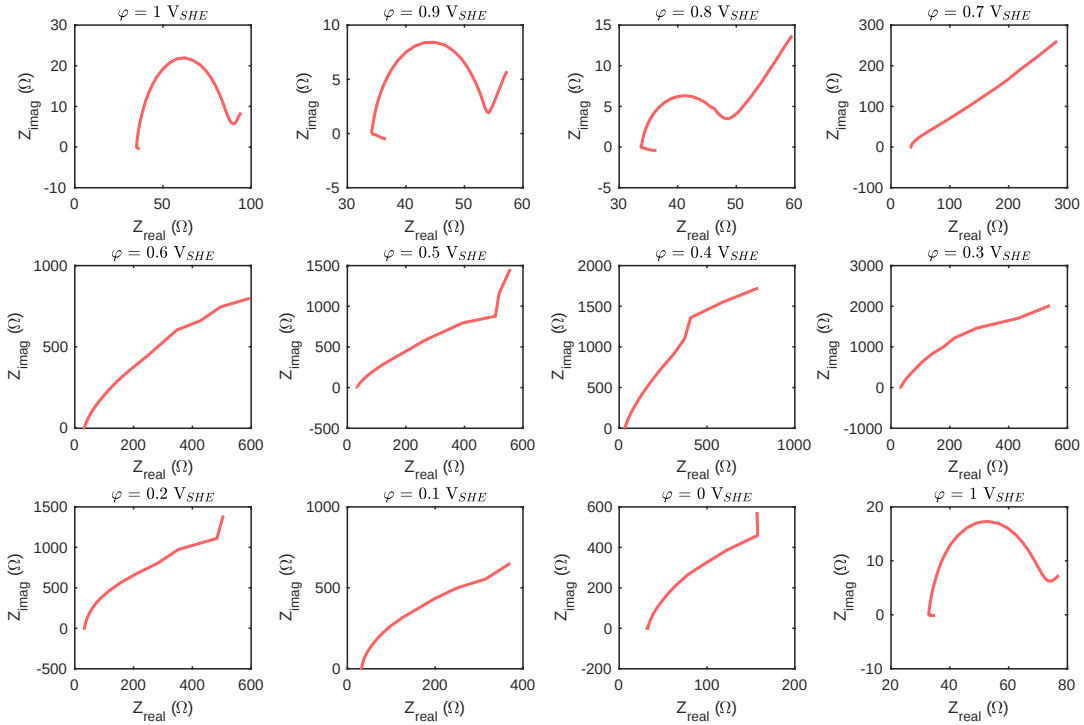

Figure S3: Nyquist plots showing electrochemical impedance spectroscopy measurements for a Au electrode in 20 mM $HAuCl_4$ at different DC potential biasses. The measurements were made starting at $\varphi = 1\ V_{SHE}$ and stepping in 100 mV increments to 0 V_{SHE}. The bottom right plot is a repeat of $\varphi = 1\ V_{SHE}$ after the other measurements to confirm the electrode did not significantly change during the measurements.

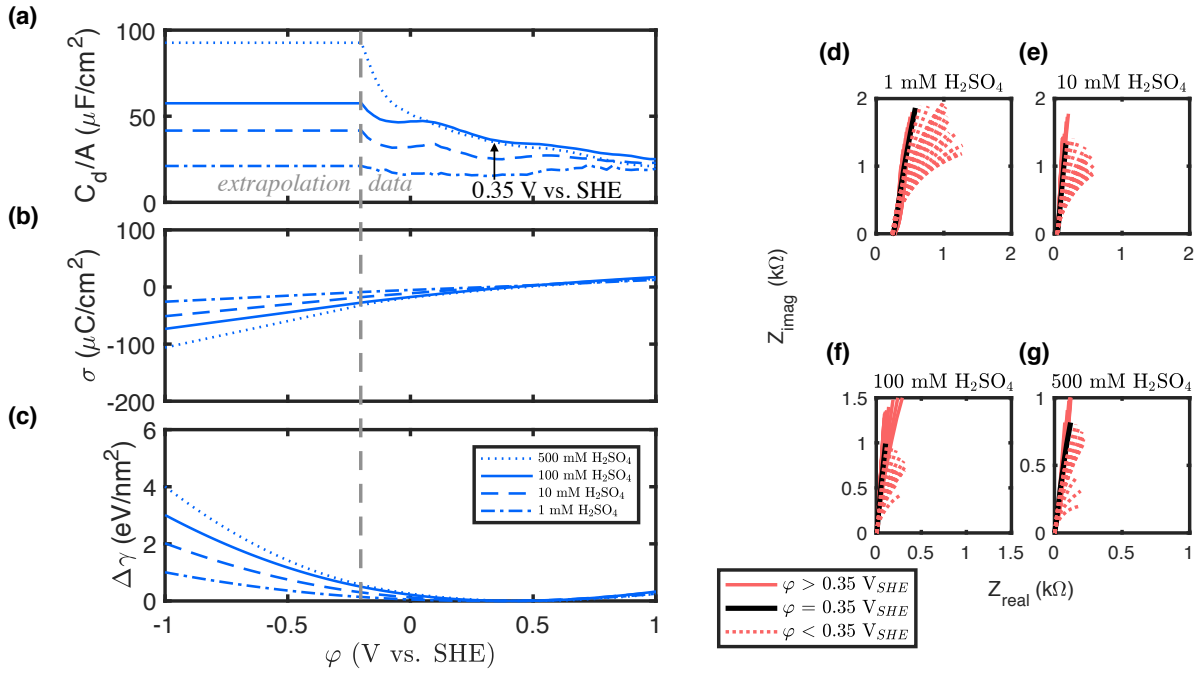

Figure S4: Potentiostatic EIS of a sputtered Au surface with geometric area 0.8 cm^2 in various concentrations of H_2SO_4. (a–c) Left of gray dashed line is extrapolation of C_d as a constant vs. φ, right of the gray dashed line is measured data. (a) C_d per unit area vs. φ; electrode area A was measured by CV of the Au in H_2SO_4. (b) σ vs. φ calculated from (a). (c) $\Delta\gamma$ vs. φ calculated from (b). (d–g) Nyquist plots of the EIS measurements at each φ, for each of the H_2SO_4 concentrations. Red solid lines are positive of 0.35 V_{SHE}, the black solid lines are at 0.35 V_{SHE}, and the dashed red lines are negative of 0.35 V_{SHE}.

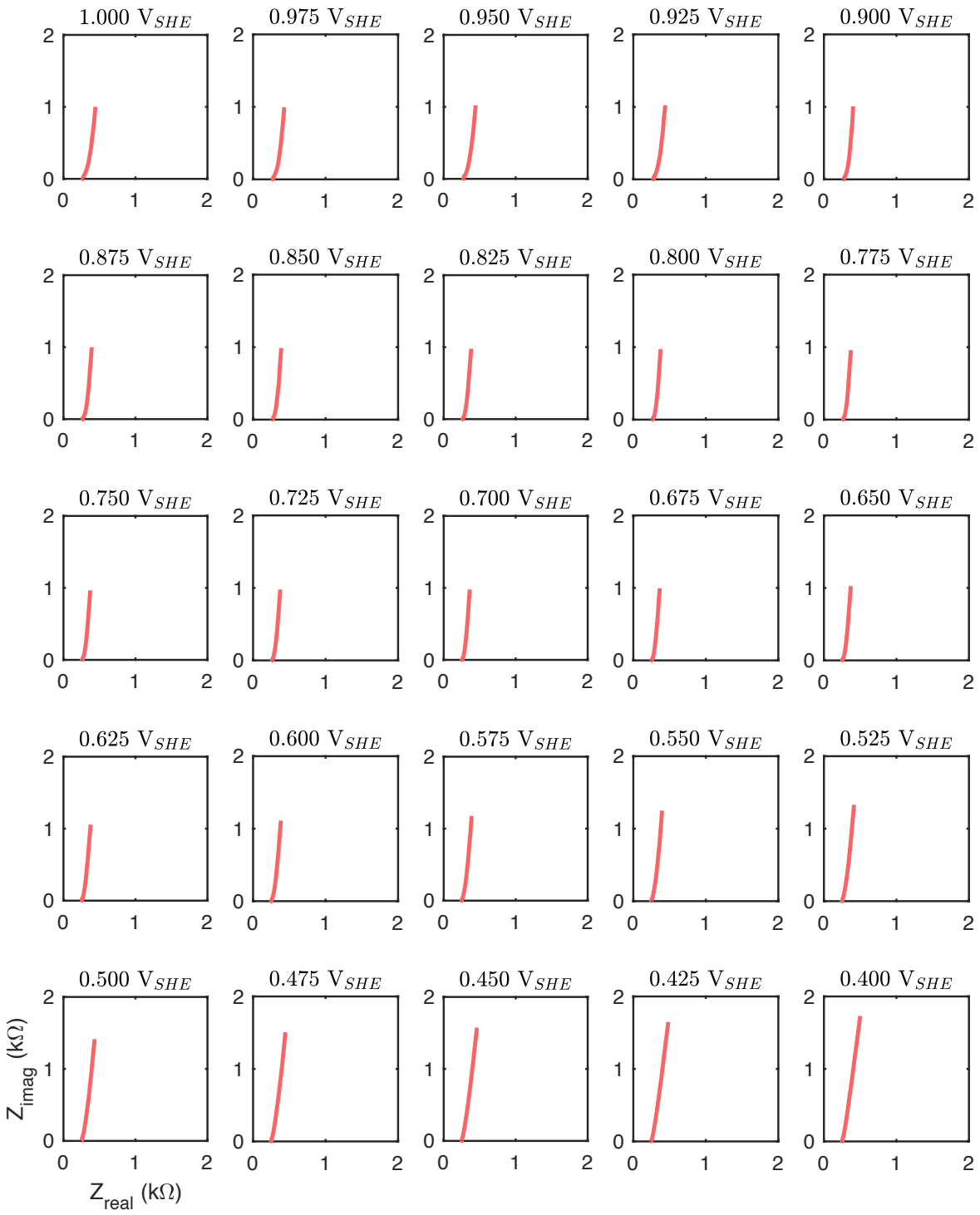

Figure S5: Nyquist plots of potentiostatic EIS measurements made in 1 mM H_2SO_4(aq) from 1 V_{SHE} to 0.4 V_{SHE}.

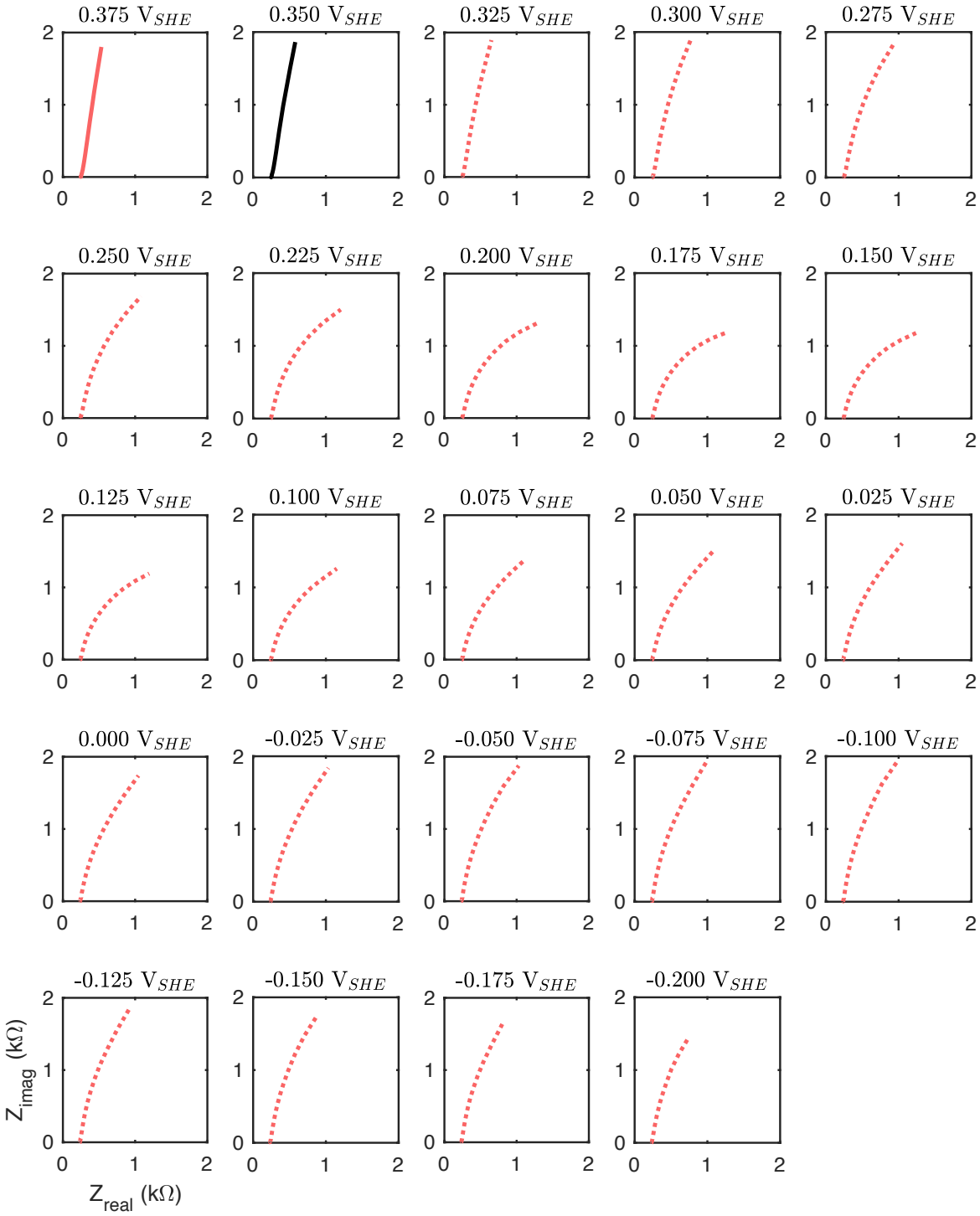

Figure S6: Nyquist plots of potentiostatic EIS measurements made in 1 mM H_2SO_4(aq) from 0.375 V_{SHE} to -0.2 V_{SHE}.

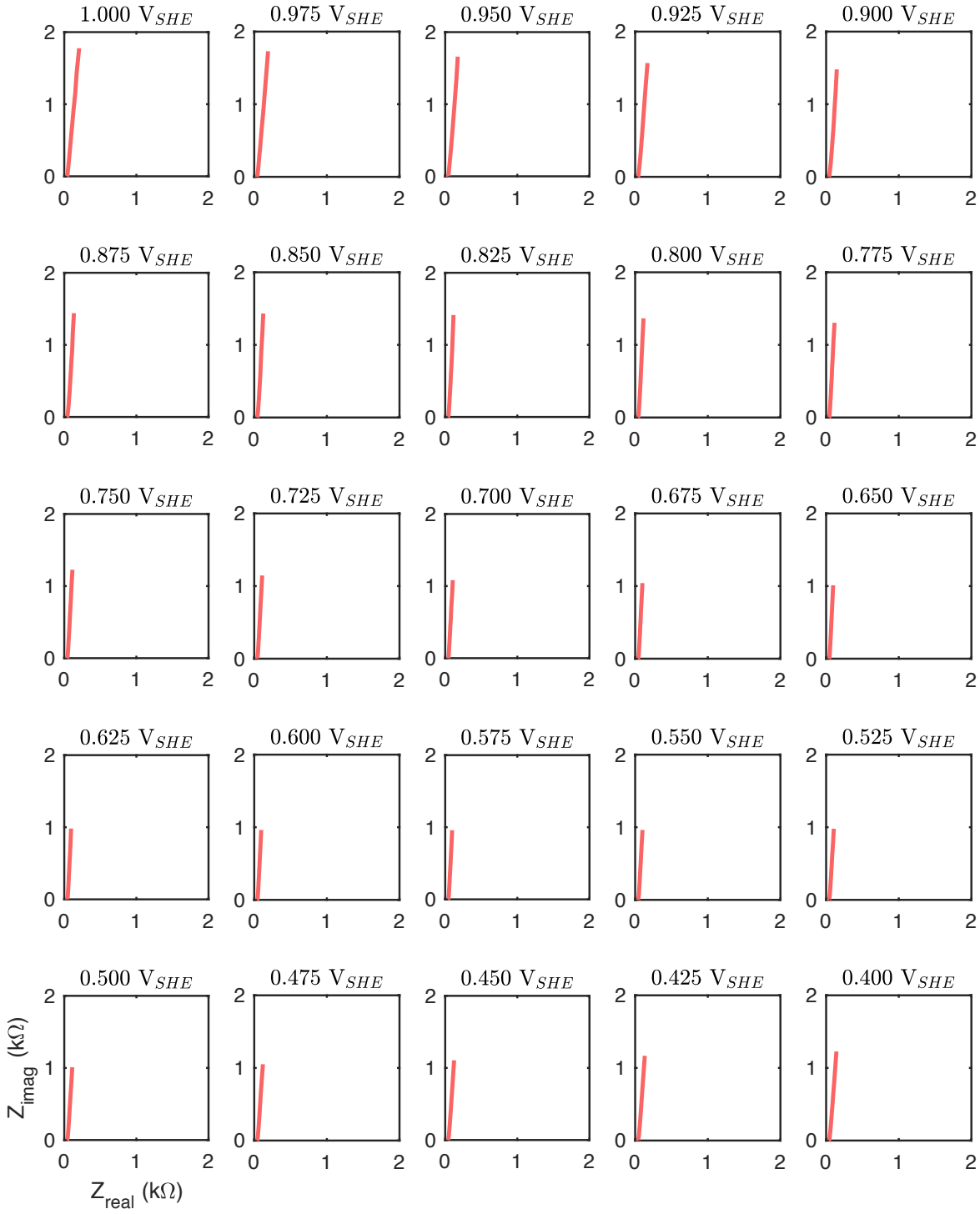

Figure S7: Nyquist plots of potentiostatic EIS measurements made in 10 mM H_2SO_4(aq) from 1 V_{SHE} to 0.4 V_{SHE}.

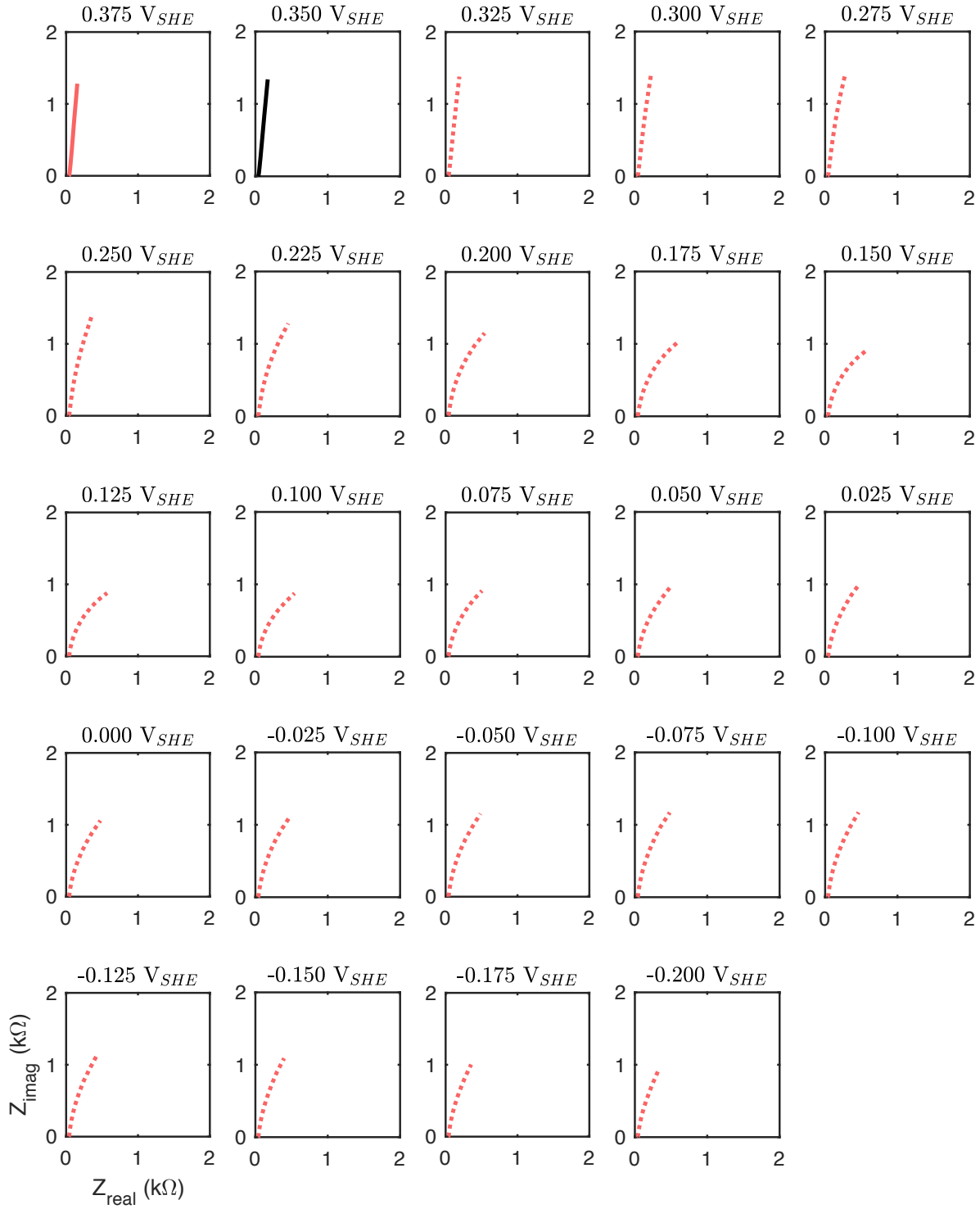

Figure S8: Nyquist plots of potentiostatic EIS measurements made in 10 mM H_2SO_4(aq) from 0.375 V_{SHE} to −0.2 V_{SHE}.

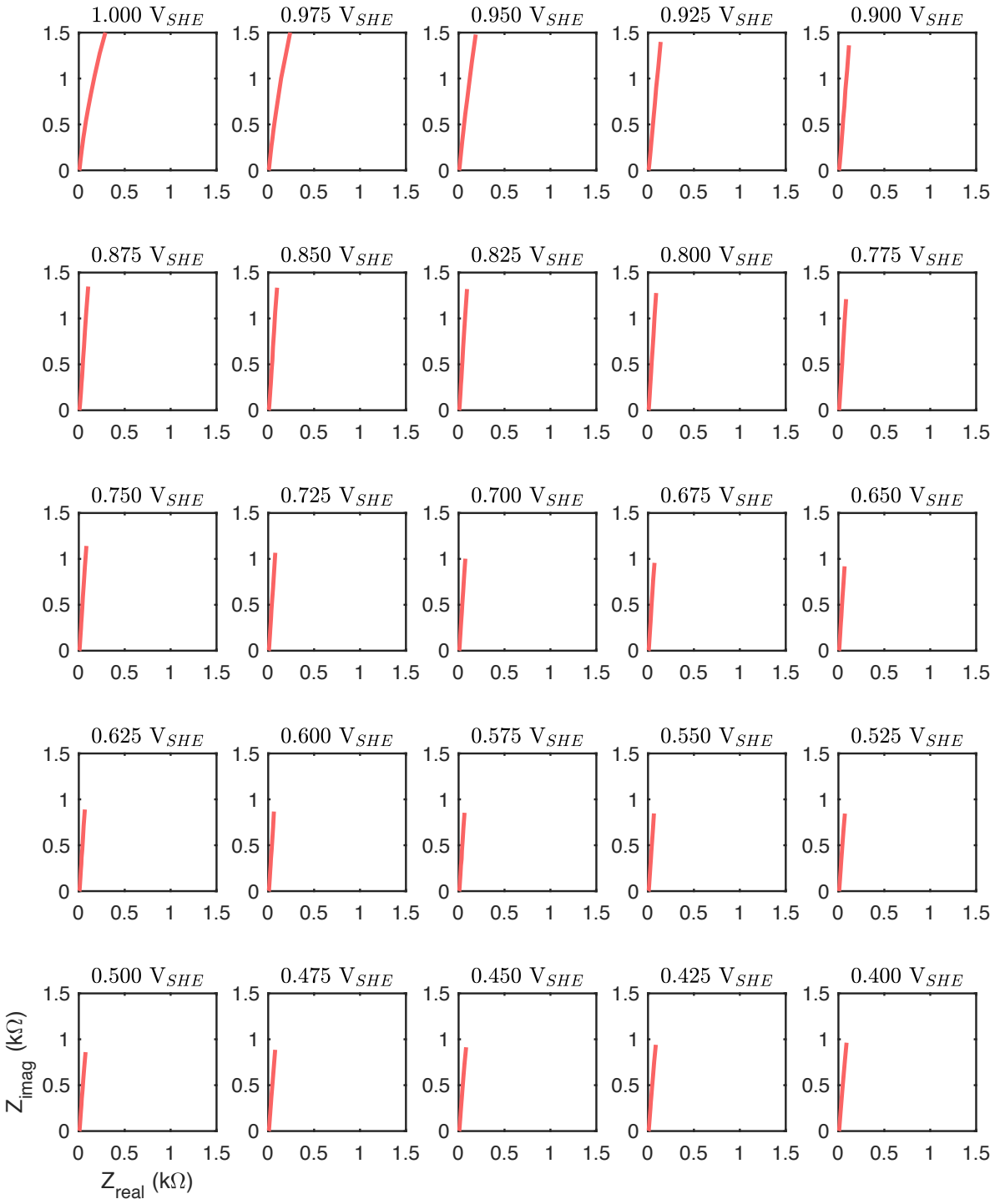

Figure S9: Nyquist plots of potentiostatic EIS measurements made in 100 mM H_2SO_4(aq) from 1 V_{SHE} to 0.4 V_{SHE}.

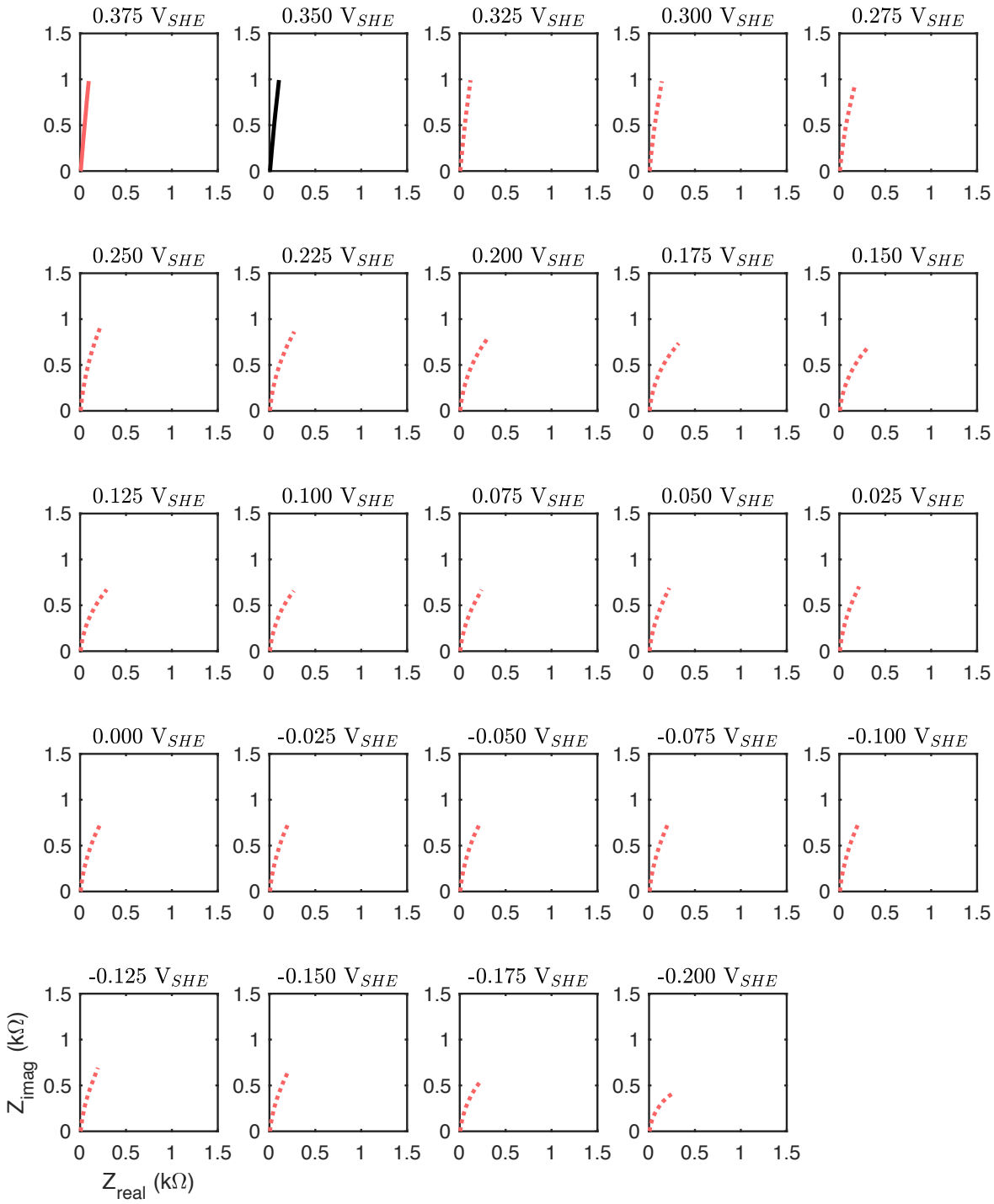

Figure S10: Nyquist plots of potentiostatic EIS measurements made in 100 mM H_2SO_4(aq) from 0.375 V_{SHE} to -0.2 V_{SHE}.

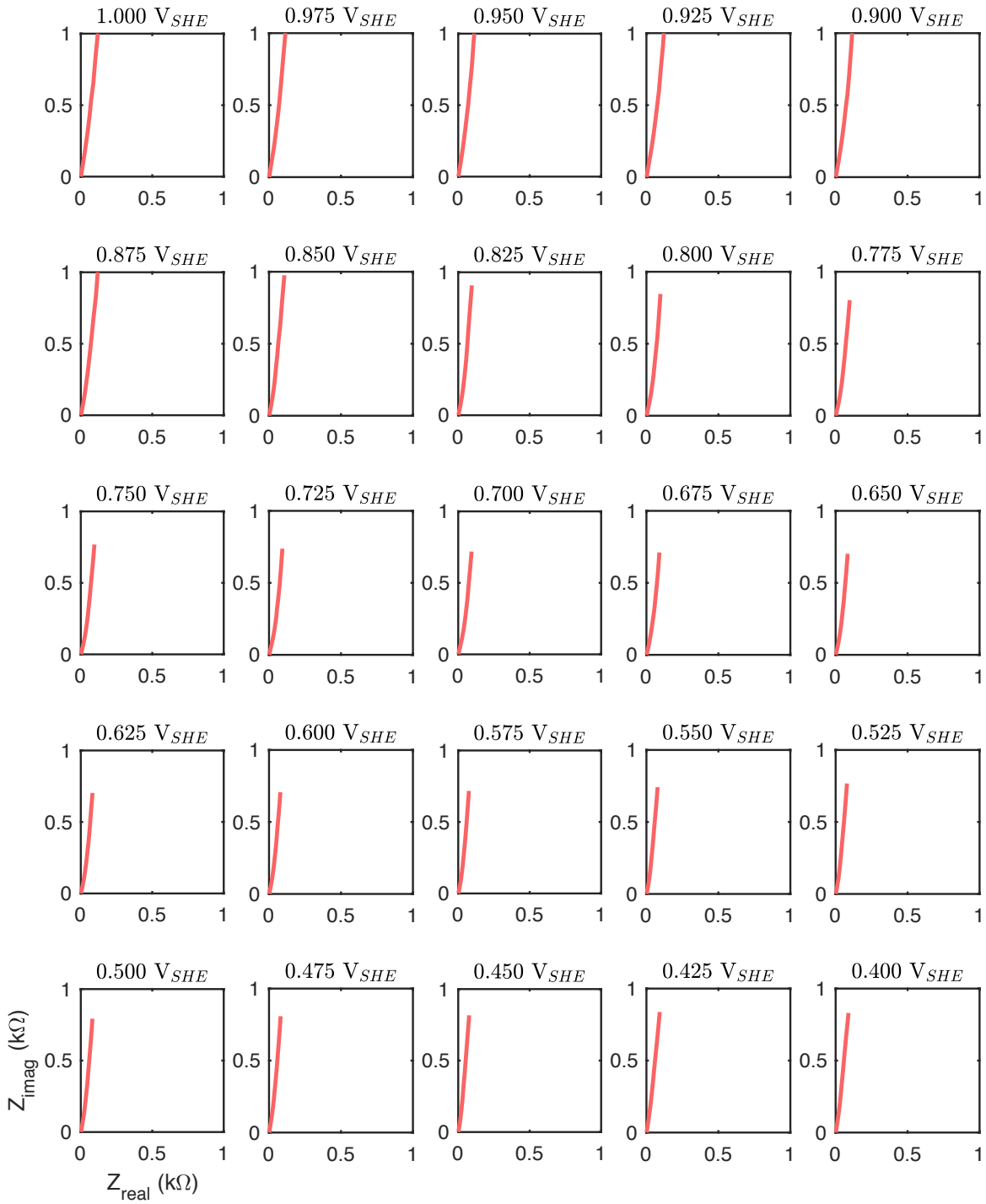

Figure S11: Nyquist plots of potentiostatic EIS measurements made in 500 mM H_2SO_4(aq) from 1 V_{SHE} to 0.4 V_{SHE}.

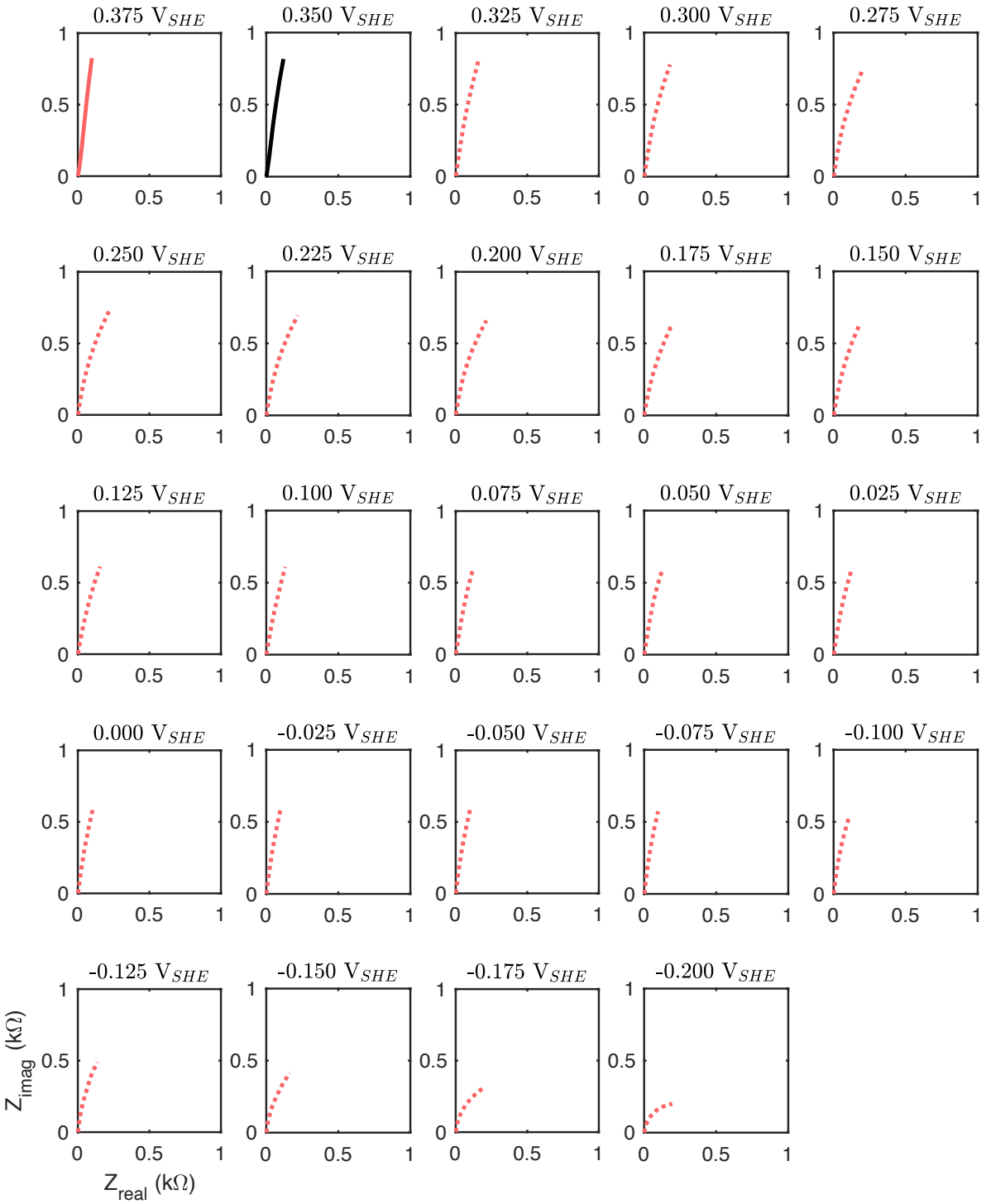

Figure S12: Nyquist plots of potentiostatic EIS measurements made in 500 mM H_2SO_4(aq) from 0.375 V_{SHE} to -0.2 V_{SHE}.

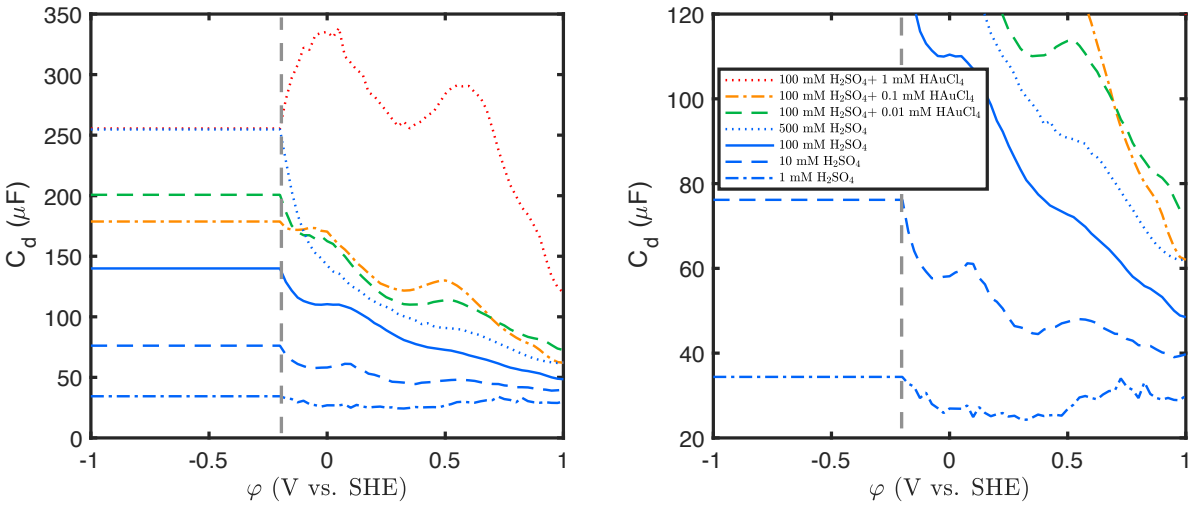

Figure S13: Net C_d vs. φ for potentiostatic EIS of a sputtered Au surface with geometric area 0.8 cm^2 in various concentrations of H_2SO_4. (left) All EIS measurements. (right) Magnified view of the pure H_2SO_4 electrolytes. Left of gray dashed line is extrapolation of C_d as a constant vs. φ, right of the gray dashed line is measured data.

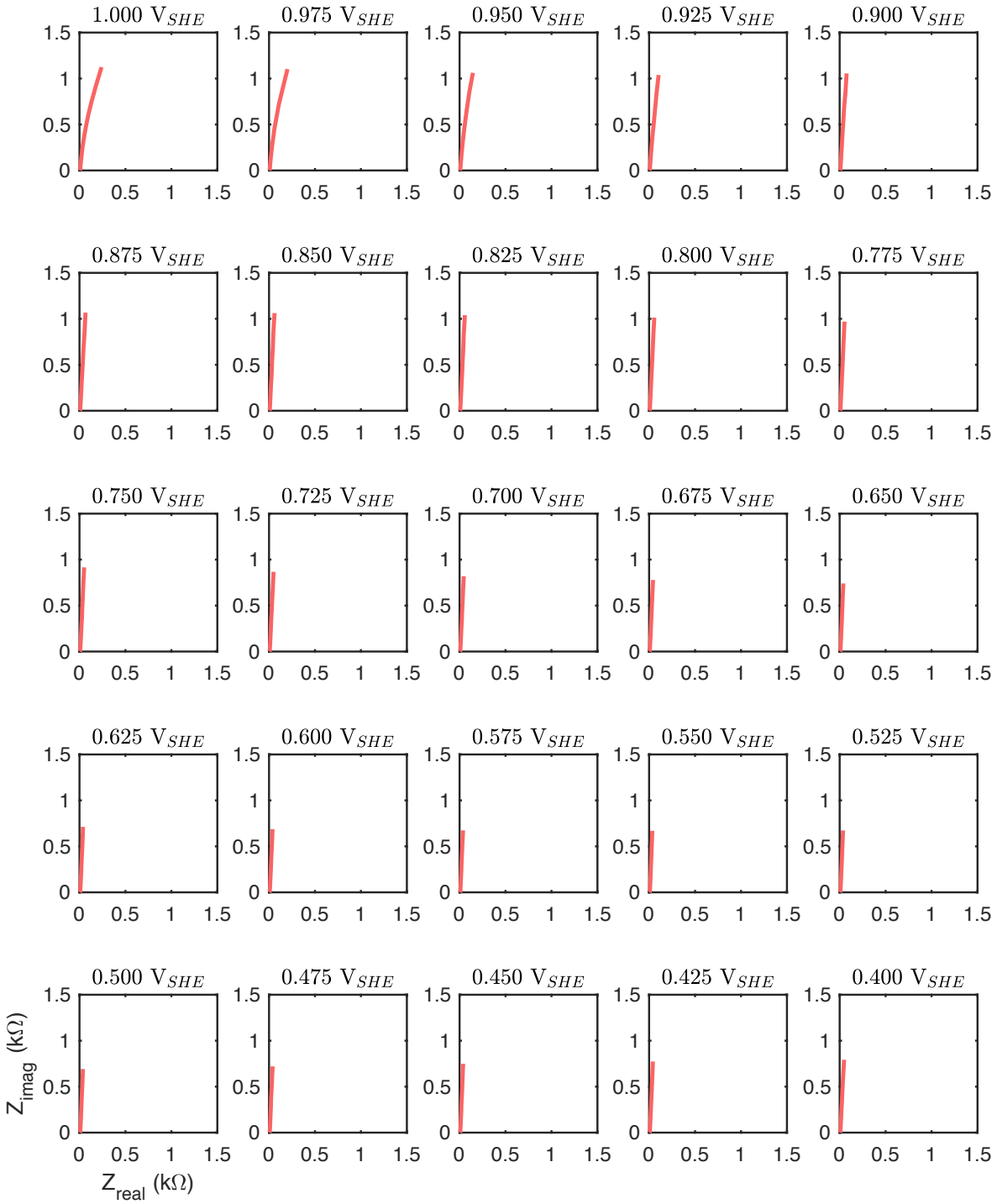

Figure S14: Nyquist plots of potentiostatic EIS measurements made in 0.01 mM $HAuCl_4$(aq) + 100 mM H_2SO_4(aq) from 1 V_{SHE} to 0.4 V_{SHE}.

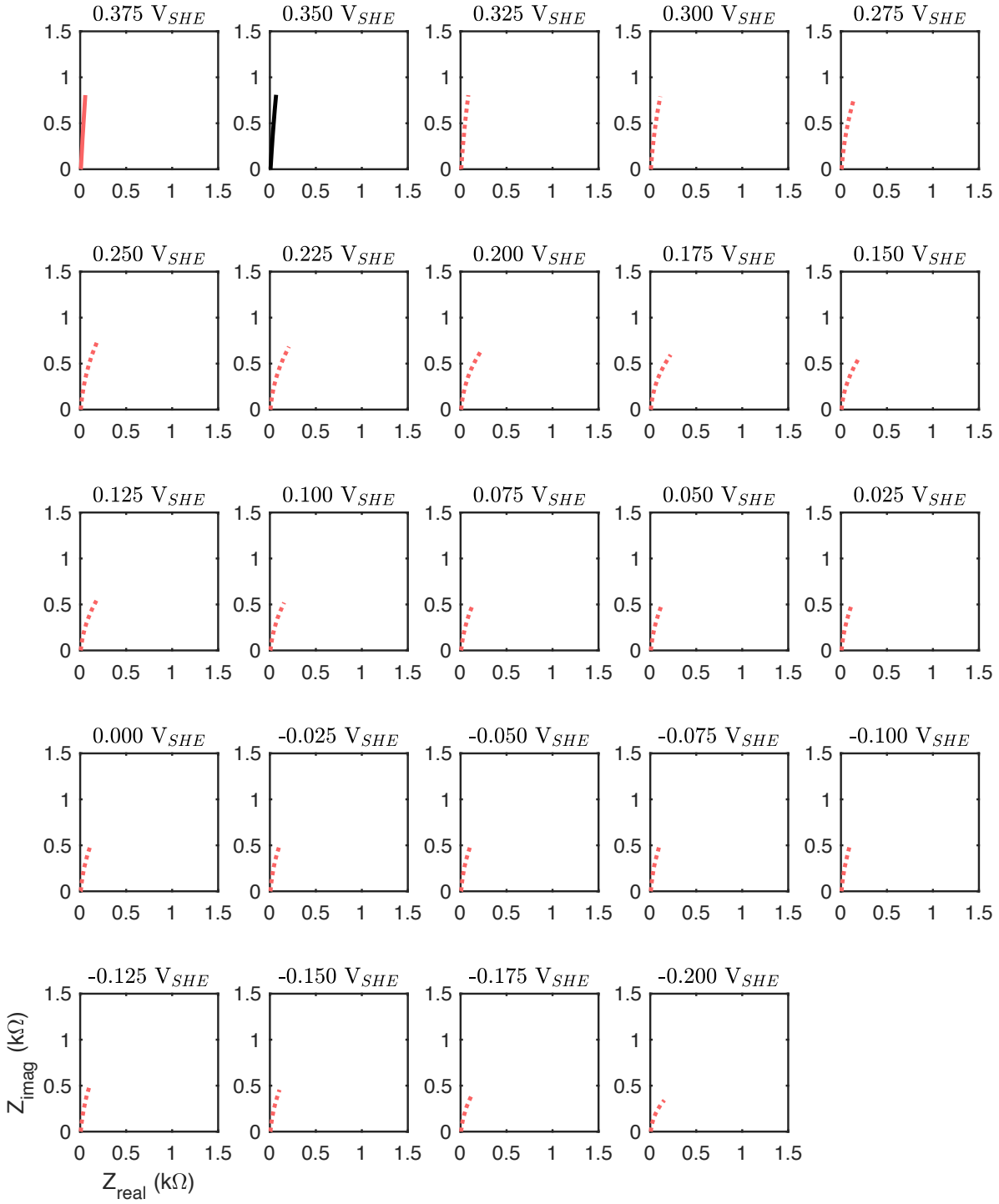

Figure S15: Nyquist plots of potentiostatic EIS measurements made in 0.01 mM $HAuCl_4$(aq) + 100 mM H_2SO_4(aq) from 0.375 V_{SHE} to −0.2 V_{SHE}.

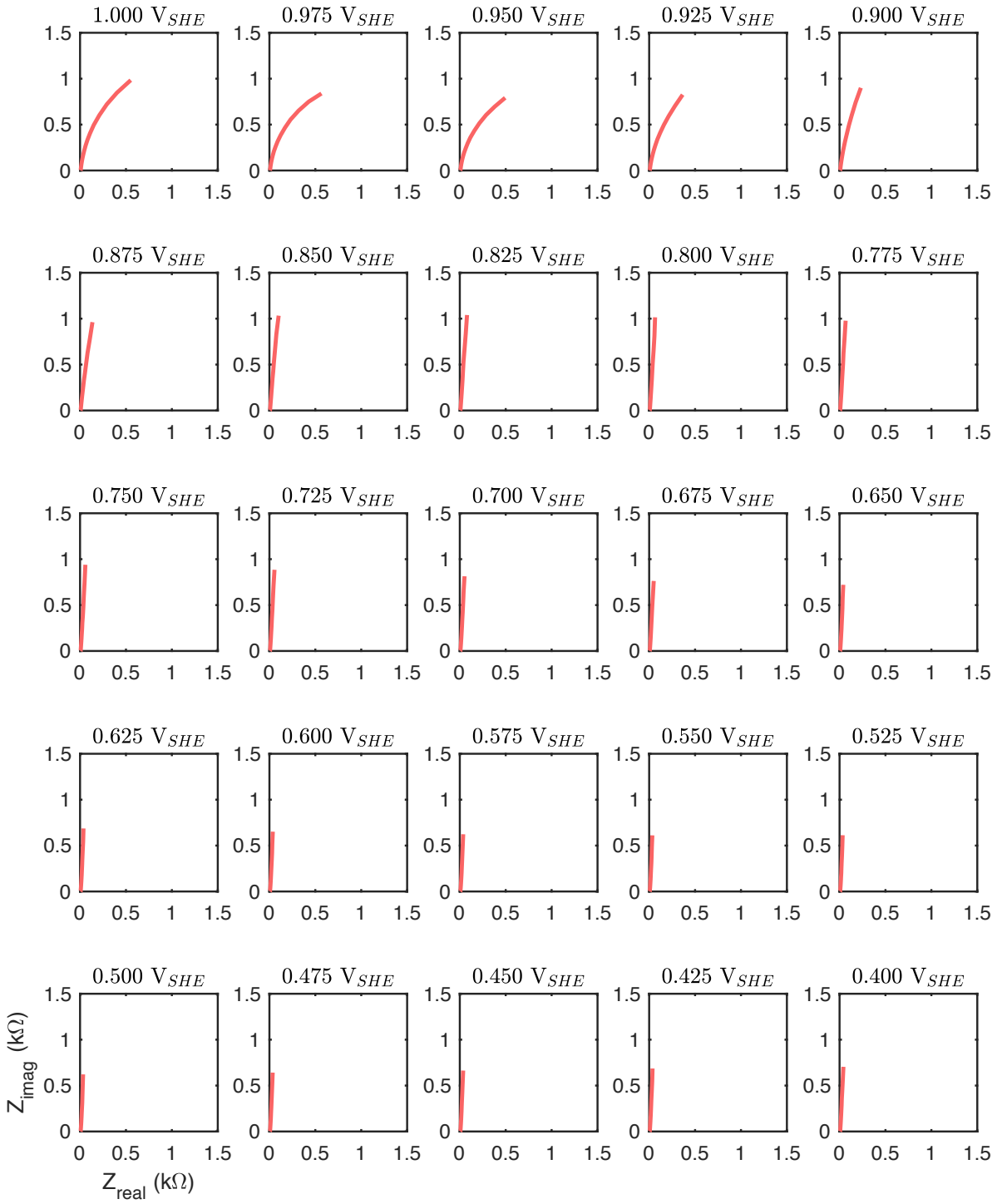

Figure S16: Nyquist plots of potentiostatic EIS measurements made in 0.1 mM $HAuCl_4$(aq) + 100 mM H_2SO_4(aq) from 1 V_{SHE} to 0.4 V_{SHE}.

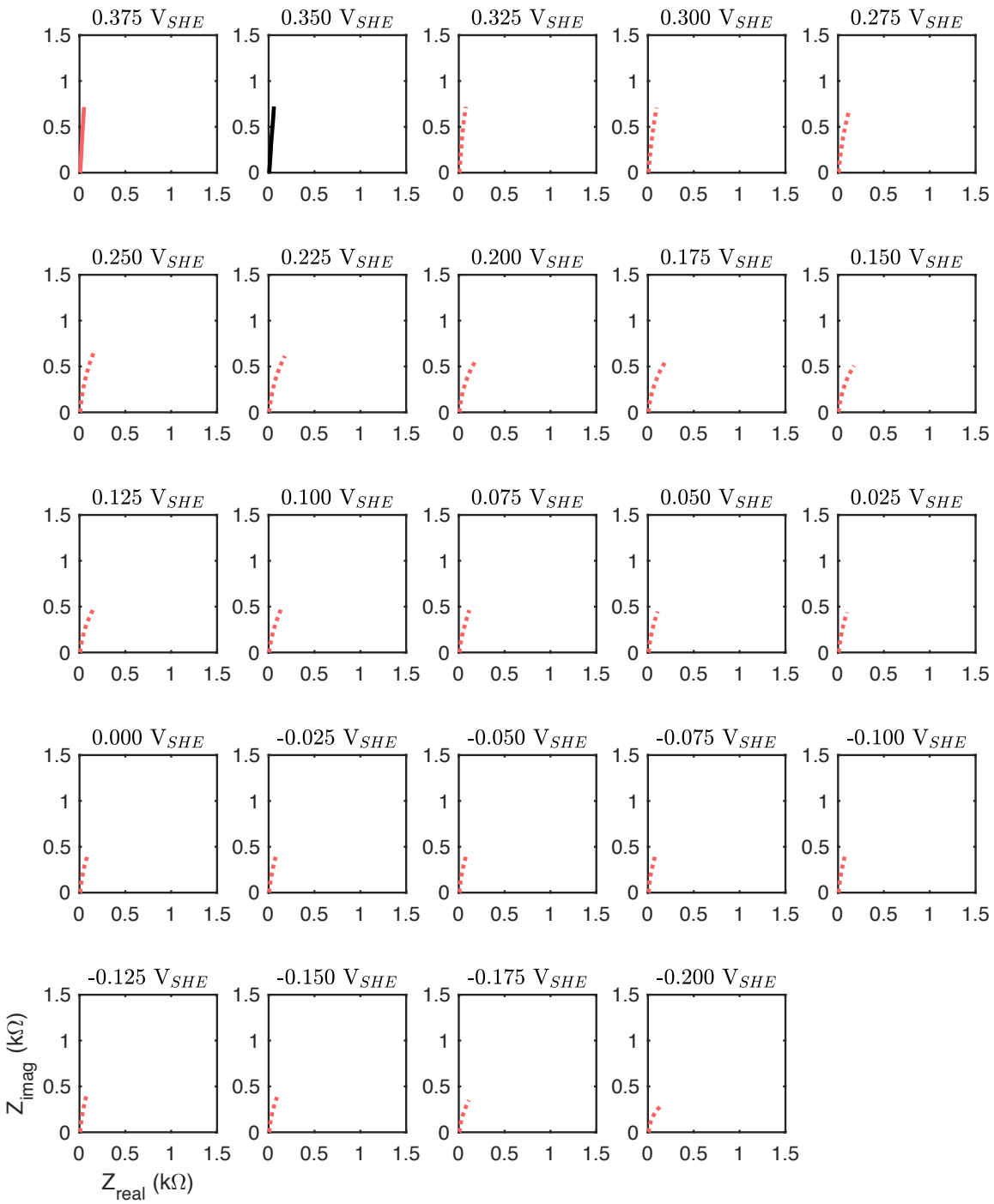

Figure S17: Nyquist plots of potentiostatic EIS measurements made in 0.1 mM $HAuCl_4$(aq) + 100 mM H_2SO_4(aq) from 0.375 V_{SHE} to −0.2 V_{SHE}.

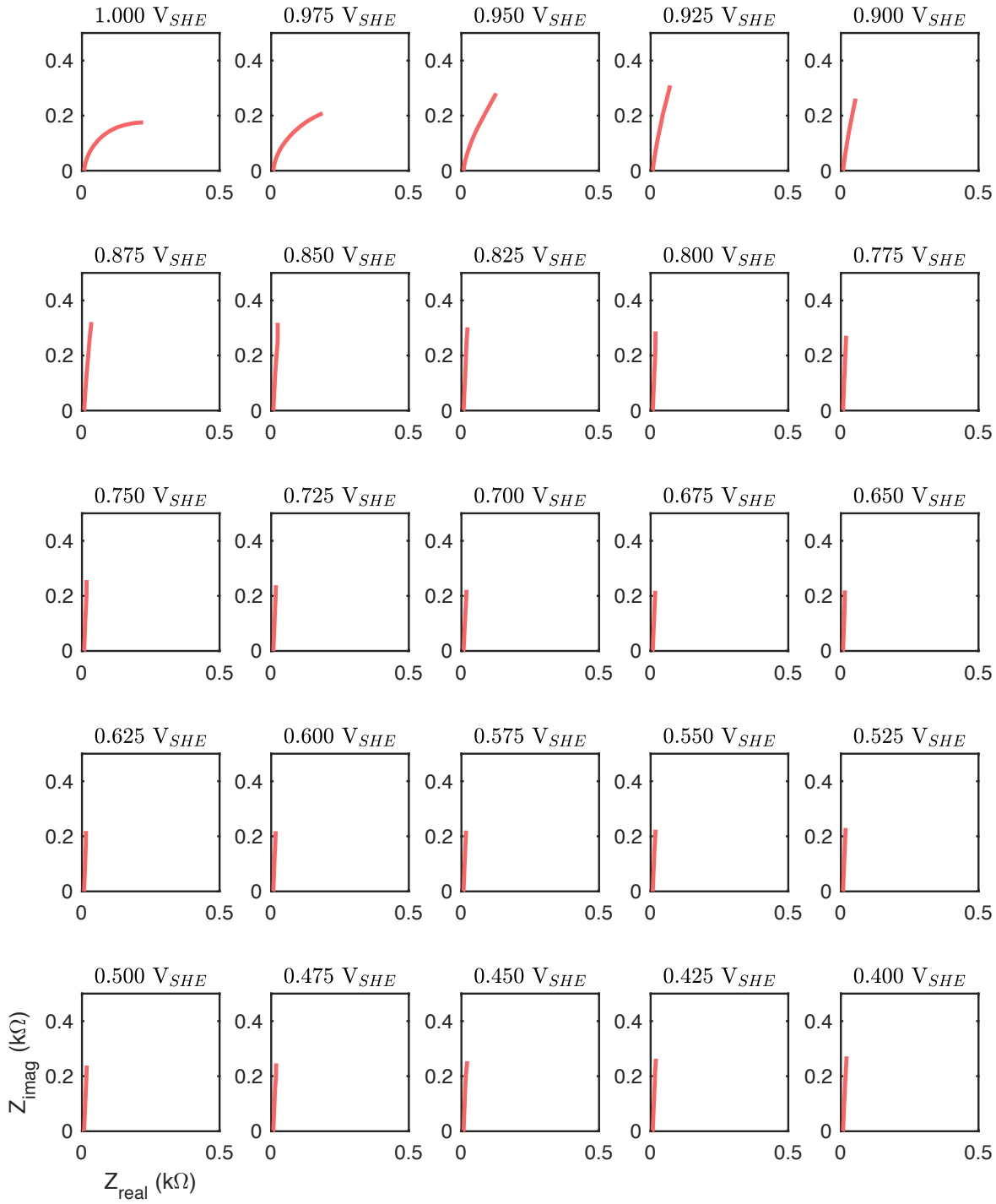

Figure S18: Nyquist plots of potentiostatic EIS measurements made in 1 mM $HAuCl_4$(aq) + 100 mM H_2SO_4(aq) from 1 V_{SHE} to 0.4 V_{SHE}.

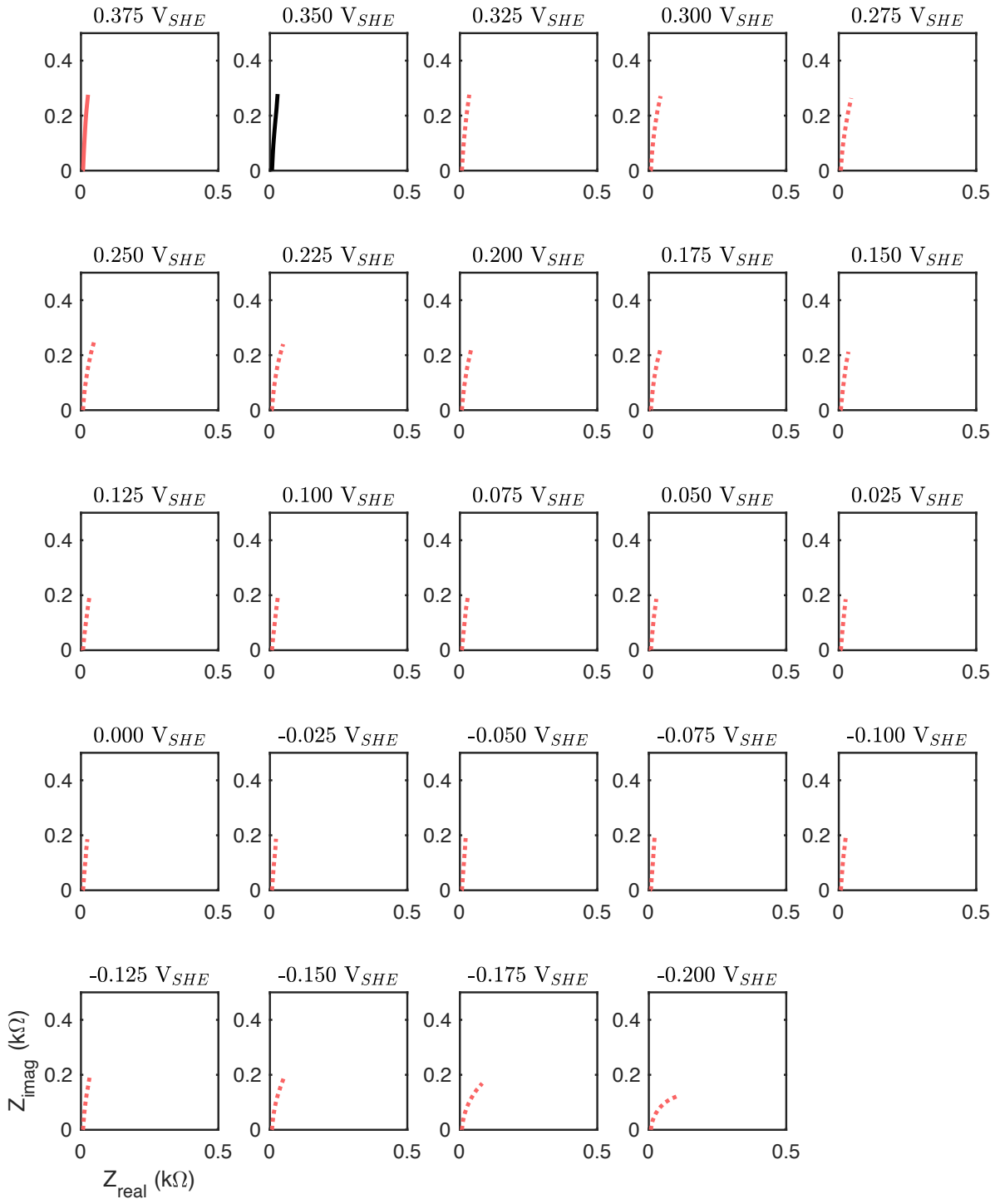

Figure S19: Nyquist plots of potentiostatic EIS measurements made in 1 mM $HAuCl_4$(aq) + 100 mM H_2SO_4(aq) from 0.375 V_{SHE} to −0.2 V_{SHE}.

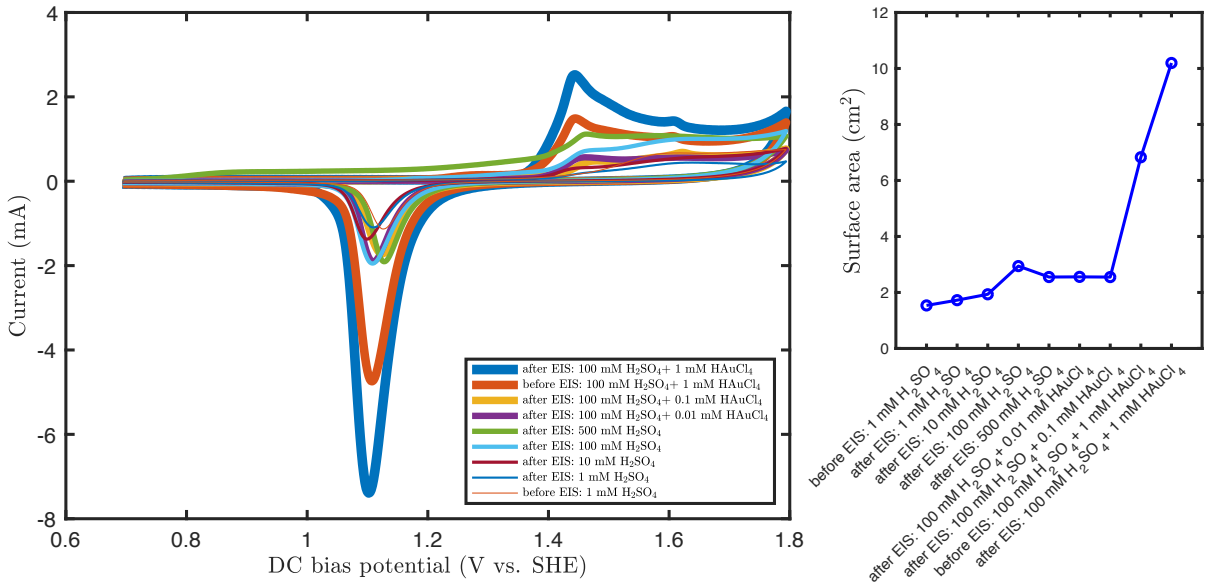

Figure S20: Cyclic voltammetry of a Au-coated Ti foil with geometric area 0.8 cm^2 in 500 mM sulfuric acid for variable concentration of H_2SO_4 and 375 mM sulfuric acid for variable concentration of $HAuCl_4$. (left) Overlayed cyclic voltammograms taken before or after EIS measurements for indicated electrolytes. (right) Real surface area of the electrode, calculated by integrating the total charge of the Au reduction peak for each curve and normalizing relative to reduction peaks of sputtered Au on a flat silicon wafer.

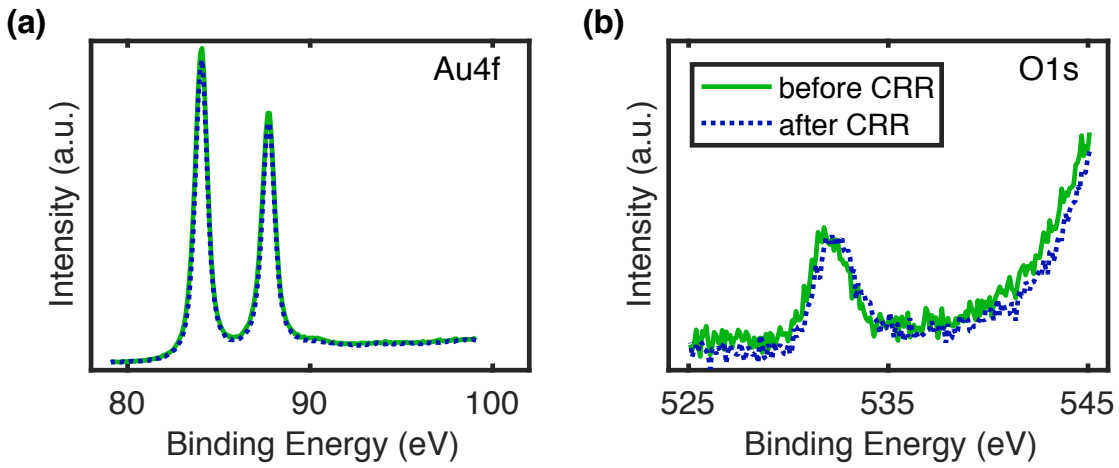

Figure S21: XPS spectrum of Au dendrites before and after the CO_2 reduction experiment with -25 mV steps. (a) The Au4f peak, (b) the O1s peak.

References

(1) Bard, A. J.; Faulkner, L. R. *Electrochemical Methods*, 2nd ed.; John Wiley & Sons, Inc.: New York, 2001.